Validation of Surface Energy Balance System (SEBS) over forest land cover and sensitivity analysis of the model

Anupam Badola
March, 2009

Course Title: Geo-Information Science and Earth Observation for Environmental Modelling and Management

Level: Master of Science (Msc)

Course Duration: September 2007 - March 2009

Consortium partners: University of Southampton (UK)
Lund University (Sweden)
University of Warsaw (Poland)
International Institute for Geo-Information Science and Earth Observation (ITC) (The Netherlands)
GEM thesis number: 2007-21

Validation of Surface Energy Balance System (SEBS) over forest land cover and sensitivity analysis of the model

by

Anupam Badola

Thesis submitted to the International Institute for Geo-information Science and Earth Observation in partial fulfilment of the requirements for the degree of Master of Science in Geo-information Science and Earth Observation for Environmental Modelling and Management

Thesis Assessment Board

Name Examiner 1	Dr. Ir. Chris M. Mannaerts (Chair)
Name Examiner 2	Ir. Wim J. Timmermans
External Examiner	Prof. Dr. Petter Pilesjö
Primary Supervisor	Dr. Ir. Christiaan van der Tol
Second Supervisor	Prof. Dr. Ing. Wouter Verhoef

ITC

International Institute for Geo-Information Science and Earth Observation
Enschede, The Netherlands

Disclaimer

Abstract

In order to estimate evapotranspiration over regional scale, a Surface Energy Balance System (SEBS) has been developed recently. SEBS is a powerful tool to estimate actual evapotranspiration over local, regional and continental scale using remote sensing and standard meteorological data. It is based on the principle of surface energy balance closure, and variables such as net radiation, soil heat flux, etc. have been parameterized in the model. SEBS calculates evapotranspiration using optical and thermal remote sensing beside weather station data.

In this study, SEBS was for the first time tested for forest land cover over the central part of the Netherlands using high resolution remote sensing data of ASTER. Besides, four methods for calculation of fractional cover and two methods for calculation of soil heat flux were validated using ground data.

Results showed that the method proposed by Gutman and Ignatov is the best of the tested algorithms for retrieval of fractional vegetation cover from remote sensing data. The two methods validated for soil heat flux estimation showed that both of them were overestimating the soil heat flux. Comparison of the estimated evaporative fraction with validation data confirms that SEBS can estimate evaporative fraction with RMSE 0.47 [-]. However, there are huge differences in the estimation of sensible and latent heat flux RMSE >50 Wm^{-2}. It has been found that image resolution (90m ASTER data) did not have any impact on the accuracy of results. It was assumed that it is due to large fetch of flux tower, (300-500m^2) used for validation.

Sensitivity analysis of the SEBS model was carried out on remote sensing inputs to SEBS model. Results show that amongst surface albedo, emissivity, land surface temperature, fractional vegetation cover and NDVI, the SEBS model is most sensitive to land surface temperature with sensible heat increasing with exponential rate beyond 35^0C surface temperature and decreasing exponentially below 20^0C. This exponential increase/decrease in sensible heat results in abrupt changes in evaporative fraction.

Acknowledgements

First of all, I would like to thank almighty god for blessing and support rendered to me towards my thesis.

I would like to thank European Union and Erasmus Mundus scholarship programme for making this M.Sc. feasible. My sincere gratitude is to the all universities of the consortium and the academic staff for providing a rich academic experience.

I would like to express my sincere gratitude to my supervisors Dr. Ir. Christiaan van der Tol and Dr. Ing. Wouter Verhoef for their guidance throughout the thesis by building logical thinking on the topic, supervision during field visit and feedback on results and discussions. I would like to thank Dr. Z. Su and Ir. Gabriel Norberto Parodi for their comments and recommendations. I would also like to thank the committee member of the thesis: Dr Andre Kooiman and Dr. Petter Pilesjö for their valuable suggestions. The valuable suggestions from Dr. Thomas Hickler (Lund University, Sweden) were highly appreciated.

I would like to thank Mr. Gerard Reinink (information technology department) for providing the ASTER data. My special thanks to Mr. Henk Wilbrink and Mr. A.S. (Benno) Masselink for providing scientific instruments for field data collection. I would like to thank Ir. Bert Heusinkveld and the supporting staff of Meteorology and Air Quality section at Wageningen University and Research Center for providing flux data for Haarweg site. My sincere thanks to Ing. Murat Ucer (ITC), Arnoud Frumau (ECN) and Arien Stolk (RIVM) for having an opportunity to use the Speulderbos flux data for validation of SEBS. Thanks to Dr. Jan Elbers, Dr. Eddy Moors and Dr. Wilma Jans of Alterra, the Netherlands for providing Loobos flux data. Special thanks to my friend Parag Khavakar for helping me during field visit.

I would like to thank my wife for being so supportive throughout the M.Sc. course and making the entire 18 months period so special to me.

Last but not the least, I express my special thanks to all the GEM students. It was a wonderful and memorable time spent together. It was a great experience of knowing each other and mutual learning during team work.

Table of contents

List of figures

List of tables

List of Acronyms

ASTER	Advanced Spaceborne Thermal Emission and Reflection Radiometer
CWSI	Crop Water Stress Index
DHP	Digital Hemispherical Photography
EF or Λ	Evaporative Fraction
EOS	Earth Observing System
G	Soil heat flux (W/m2)
GCPs	Ground Control Points
GER	Geophysical and Environmental Research Corporation
GLA	Gap Light Analyzer
GMT	Greenwich Mean Time
GPS	Global Positioning System
H	Sensible heat flux (W/m2)
HDF	Hierarchical Data Format
LAI	Leaf Area Index (m^2/m^2)
λE or LE	Latent heat flux (W/m2)
LP DAAC	Land Processes Distributed Active Archive Centre
LST	Land Surface Temperature
MLNI	Modified Non Linear vegetation Index
NDVI	Normalized Difference Vegetation Index
NOAA	National Oceanic and Atmospheric Administration
RMSE	Root Mean Square Error
R_n	Net incoming solar radiation at surface (W/m2)
RRMSE	Relative Root Mean Square Error
SDVI	Scaled Difference Vegetation Index
SEBAL	Surface Energy Balance Algorithm for Land
SEBS	Surface Energy Balance System
TES	Temperature and Emissivity Separation
UTM	Universal Transverse Mercator
WDI	Water Deficit Index

1. Introduction

1.1. Background and significance

Surface energy balance closure, more specifically, net radiation at earth's surface, latent heat (*LE*) and sensible heat (*H*) play key role in the exchange of mass and energy between land and atmosphere. The global annual average of *LE* and H is 85 W/m^2 (25% of primary solar radiation) and 19W/m^2 (6% of primary solar radiation) respectively (Ohmura, 2005). The major part of solar radiation is the latent heat flux which is basically evaporated water from land surfaces (evapotranspiration) multiplied with latent heat of vaporisation of water (a constant). It has been well established that evapotranspiration is a connecting link between both energy and water cycle. Evapotranspiration is required to quantify in order to understand the ecosystem functionality, plant primary productivity, climate change and water availability on local, regional and continental scale.

Point measurements of evapotranspiration are possible but it is impractical to measure every point in the field consequently cost effective methods such as water balance approach, mass transfer approach, eddy correlation, energy balance, combination approach, etc have been developed to estimate evapotranspiration on small homogenous areas (Hall, 1992; Singh, 1995). Above-mentioned methods have limitation in extrapolating results on a large area because of land heterogeneity, vegetation and topography (Betts and Beljaars, 1993; Dingman, 2002). In order to estimate evapotranspiration over a large area, the energy balance approach coupled with satellite data seems a promising solution (Bastiaanssen et al., 1998; French et al., 2005; Li et al., 2008).

The process of evapotranspiration is governed by energy. Since a lot of energy is consumed for vaporization of water, the evapotranspiration, in a local, regional or global scale, consumes a significant amount of solar flux falling on the surface and changes significantly with seasons as per water and energy availability. Some of the basic concepts behind surface energy balance approach are as follows:

The energy balance approach starts with the universal surface energy balance equation (Su, 2002). It can be mathematically expressed as equation 1.1.

$$R_n = G + H + \lambda E \tag{1.1}$$

In equation 1.1, R_n is the net radiation falling on the land surface [Wm^{-2}], G is soil heat flux [Wm^{-2}], H is the turbulent sensible heat flux [Wm^{-2}] and λE is latent heat flux [Wm^{-2}] where λ is the latent heat of water [Jkg^{-1}]. It is important to mention that energy consumed in photosynthesis is very small compared to the other terms and that's why it is neglected in the equation (French et al., 2005). In order to estimate the latent heat flux, many equations and algorithms have been developed in the past (Verstraeten et al., 2005).

1.2. Previous work carried out in energy balance approach

Estimation of evapotranspiration was first of all represented by Penman by combination of the energy balance equation with the equation for aerodynamic water vapour transfer (Su, 2005). Later on, Monteith modified the equation by including canopy resistance for diffusion of vapour. The equation is well known as Penman-Monteith combination approach. Later on, Jackson et al. developed Crop Water Stress Index (CWSI) using canopy temperature, air temperature and net radiation (Su, 2005). Moran et al. (1994) introduced Water Deficit Index (WDI) for estimation of evapotranspiration for fully vegetated to partially vegetated land surfaces. Further development in this area was the Surface Energy Balance Index (Menenti and Choudhury, 1993) which became a foundation for the remote sensing based surface energy balance approach.

At present, many algorithms, such as Surface Energy Balance Algorithm for Land (SEBAL) and Surface Energy Balance System (SEBS) have been developed for estimation of evapotranspiration at regional scale and were validated successfully in various ecosystem types. For instance, Su (2002) validated the SEBS model for maize, fallow land & bare soil and found the difference between measured and estimated evapotranspiration by 14% for maize. Bastiaanssen et al. (1998) reported the accuracy of SEBAL for arid zones from 81 to 95% in estimation of evaporative fraction. Verstraeten et al. (2005) estimated actual evapotranspiration using NOAA imagery over 14 European forest sites. The Root Mean Square Error (RMSE) and Relative Root Mean Square Error (RRMSE) of ET_{NOAA} and $ET_{Euroflux}$ was compared after calculating soil heat flux (G) using two different approaches (Bastiaanssen, 1995; Su, 2002). It is worth mentioning that the results were based on course resolution image (1.1km) analysis. Since course resolution images represent less land heterogeneity as compared to medium to high resolution images, results may vary on medium to high resolution satellite data (lders and Raabe, 1996; Li et al., 2008).

Each algorithm developed for energy balance closure on land has its own advantages and disadvantages. For example, in case of SEBS and SEBAL, SEBAL can only be applied to an area where both wetland and dry land pixels are available but it demands few input variables (Bastiaanssen et al., 1998). On the other hand, SEBS provides better parameterization for surface roughness length but requires some ancillary data as well (Jia et al., 2003). Another advantage of SEBS is that the model is recently developed (2002) taking previous models into account and provides better parameterization for aerodynamic roughness length (Jia et al., 2003; Su, 2002). The SEBS algorithm is discussed in detail in Chapter 2.

1.3. Research problem

The SEBS algorithm has been validated for a number of crops (Su, 2002, French et al., 2005) using high resolution satellite data with acceptable accuracy. But it has not been validated for forests using high resolution imagery (like ASTER). Since forests are key sinks of carbon, and, if SEBS can estimate actual evapotranspiration on forest landscape, the model can be coupled with ground biomass estimation models where evaporative fraction (output of SEBS) is a key input (Verstraeten et al., 2005; Verstraeten et al., 2008).

The selection of satellite image is also very crucial for surface energy balance modelling and tt has to be consistent in quality with enough spatial resolution to distinguish land heterogeneity. This is an important point to consider as input variables of SEBS (fractional vegetation cover, land surface albedo and temperature) vary with variation in land surface variables (surface emissivity, albedo, vegetation and temperature). French et al. (2005) have shown the suitability of ASTER images regarding their spatial and spectral resolution in crop fields. The number of bands (14), dual looking view and capability to retrieve surface temperature differences near 0.5ºC with high resolution makes it suitable for surface energy balance modelling (French et al., 2005). Therefore, it is interesting to investigate the results of ASTER data on forest land cover using the SEBS model and compare the results with the study carried out by Verstraeten et al. (2005) on forest land cover using 1.1km spatial resolution.

Fractional vegetation cover is one of the important inputs in SEBS. Surface emissivities, roughness length for heat transfer and soil heat flux are parameterized as a direct function of vegetation cover in SEBS. Many attempts have been made to develop a relationship between vegetation indices and fractional cover (Jiang et al., 2006; Kimura et al., 2007). The relationships between NDVI and fractional vegetation cover are well established (Kustas et al., 1993; Ormsby et al., 1987). Mainly there are three common NDVI based methods to estimate fractional cover (Baret et al., 1995; Carlson and Reply, 1997; Gutman and Ignatov, 1998).

Jiang et al. (2006) compared fractional vegetation cover obtained by above-mentioned NDVI based methods on field data and developed a new method based on the simple ratio of red and NIR reflectance. However, results were based on field data and have not been verified on remote sensing data (Jiang et al., 2006). It is interesting to verify the findings of Jiang et al. (2006) on remote sensing data in order to use the right method for estimation of fractional vegetation cover from remote sensing data.

Similarly, there are two methods for estimation of soil heat flux from remote sensing data (Bastiaanssen et al., 1998; Su, 2002). The method proposed by Bastiaanssen et al. (1998) uses more variables then method proposed by Su (2002). It is interesting to investigate the behaviour of both the methods for high canopies (forest) and low vegetation like grass and crops as a model developed for regional scale (like SEBS) should be able to estimate soil heat flux on both land cover types. Considering above-mentioned circumstances in estimating evapotranspiration, the following general and specific objectives have been stated for the study:

1.4. Research objectives

General objective: The general objective of the research is to apply and validate the Surface Energy Balance System (SEBS) algorithm using ASTER data on forest land cover and, to look into the sensitivity of SEBS for parameters derived from remote sensing data.

1.4.1. Specific objectives

- To estimate fractional vegetation cover using four methods (Baret et al., 1995; Carlson and Ripely, 1997; Gutman and Ignatov, 1998, Jiang et al., 2006) from ASTER images and compare the methods with field estimates
- To validate soil heat flux obtained from empirical equations (Su, 2002; Bastiaanssen at al., 1998) with field data
- To estimate evapotranspiration over Veluwe region, the Netherlands using ASTER data with SEBS algorithm and its validation with field data
- To carry out sensitivity analysis of SEBS model for remote sensing data inputs

1.4.2. Research questions

1. Which method of fractional vegetation cover estimation (from remote sensing data) is close to field estimates?
2. Which empirical relationship (Su, 2002; Bastiaanssen et al., 1998) leads to better estimates of soil heat flux?
3. Are instantaneous (derived from SEBS) and mean diurnal (field data) evaporative fraction comparable? If not, how much is the deviation from the daily mean of the field data?
4. To which remote sensing input parameter, the evaporative fraction (SEBS output) is the most sensitive.

1.5. Hypothesis test

In order to fulfil the objectives and research questions, the following hypothesis have been stated:

H_0: Method proposed by Jiang et al., (2006) leads to better estimate of fractional vegetation cover.

H_1: Method proposed by Jiang et al. (2006) does not lead to better estimate of Fractional vegetation cover.

H_0: Instantaneous evaporative fraction (derived from SEBS) and mean diurnal evaporative fraction (derived from field data) are comparable.

H_1: Instantaneous evaporative fractions (derived from SEBS) and mean diurnal evaporative fraction (derived from field data) are not comparable.

1.6. Organization of thesis

The entire thesis is organized in seven chapters from introduction to conclusions and recommendations. The broad overview of remaining chapters is as follows:

Chapter 2 Surface Energy Balance System (SEBS)
This chapter explains the components of SEBS algorithm and parameterization of the model.

Chapter 3 Study area
This chapter describes the study area in detail. The land cover, climate and topography of the area is explained in this chapter.

Chapter 4 Materials and instrumentation
This chapter gives detail idea of the instruments and materials used during field data collection, the validation data used in the study along with ancillary meteorological data and ASTER scene description. The data quality is also mentioned.

Chapter 5 Methodology
This chapter describes the followed approach to meet the objectives and answer the research questions.

Chapter 6 Results and discussion
This chapter presents the results for soil heat flux, fractional cover and evaporative fraction obtained from satellite data along with the validation with field data. The sensitivity of SEBS for parameters obtained from remote sensing data is also explained.

Chapter 7: Conclusions and recommendations
This chapter represents conclusions, limitations and recommendations from the study undertaken.

2. Surface Energy Balance System (SEBS)

2.1. Net radiation

Net radiation on any point at earth surface is result of net shortwave (incoming and outgoing) and long wave (incoming and outgoing) radiation. Mathematically it can be represented as equation 2.1.

$$R_n\downarrow = (1-\alpha)R_{swd}\downarrow + \varepsilon R_{lwd}\downarrow - (\varepsilon\sigma T_0^4) \tag{2.1}$$

Where α is surface albedo [−], $R_{swd}\downarrow$ is downward solar radiation [Wm^{-2}], $R_{lwd}\downarrow$ is downward long wave radiation [Wm^{-2}], ε surface emissivity [−], σ is the Stefan-Boltzmann constant [$Wm^{-2}\ .K^4$], and T_0 is the surface temperature [K]. Depending upon land surface characteristics, part of incoming shortwave and long wave radiation gets reflected. Equation 2.1 uses albedo and emissivity to define radiation properties of land surface. It is also possible to use measured values of incoming shortwave radiation (if the area is small and whether station is available) in equation 2.1. In case of non-availability of weather station, indirect methods have been developed to calculate the incoming shortwave and longwave radiation (Verstraeten et al., 2005). The instantaneous daily incoming shortwave radiation ($R_{sed}\downarrow$) at earth surface can be calculated as:

$$R_{sed}\downarrow = \tau R_{swd}\downarrow^{exo} \tag{2.2}$$

Where $R_{swd}\downarrow^{exo}$ is instantaneous extraterrestrial solar radiation [Wm^{-2}] and is equal to 1367 Wm^{-2} (Verstraeten et al. 2005). The τ is effective transmission coefficient in the shortwave range. Due to the variation in sun earth distance, an eccentricity correction factor (E) has been introduced in equation 2.2.

$$R_{swd}\downarrow = \tau\ R_{swd}\downarrow^{exo} = 1367\ .E\ .cos\,(SZA) \tag{2.3}$$

$$\begin{aligned} E &= 1.00011 + 0.03422\cos(d_a) + 0.00128\sin(d_a) \\ &+ 0.000719\cos(d_a) + 0.000077\sin(2d_a) \end{aligned} \tag{2.4}$$

$$d_a = \frac{2\pi(d_n - 1)}{365} \tag{2.5}$$

Where d_a and d_n are day angle [radians] and day of the year respectively. *SZA* (in equation 2.3) is Solar Zenith Angle [radians]. Similarly, longwave incoming radiation can be calculated from Stephen-Boltzmann law using emissivity of standard atmosphere (Campbell and Norman, 1998):

$$R_{lwd}\downarrow = \sigma\varepsilon_a T_a^4 \tag{2.6}$$

$$\varepsilon_a = 9.2\times10^{-6}\times(T_a+273.15)^2 \tag{2.7}$$

By using equations 2.2 to 2.7, it is possible to calculate the first important variable (R_n) from equation 2.1.

2.2. Surface albedo

Liang (2002) proposed narrowband to broadband shortwave albedo (α) conversion methods for a number of satellites including ASTER. The methods are empirical relationships and developed by performing regression analysis using various satellite band combinations and field data. The relationship developed for ASTER band combinations is shown in equation 2.8.

$$\alpha_{\text{short}} = 0.484\times Band_1 + 0.335\times Band_3 - 0.324\times Band_5 + 0.551 \times Band_6 + 0.305\times Band_8 - 0.367\times Band_9 - 0.0015 \tag{2.8}$$

2.3. Soil heat flux (*G*)

The model SEBS uses fractional vegetation cover and net radiation to calculate soil heat flux assuming linear relationship between soil heat flux and net radiation (Su, 2002).

$$G = R_n\,[\Gamma_c + (1-f_c)\times(\Gamma_s - \Gamma_c)] \tag{2.9}$$

The Ratio of soil heat flux to net radiation for fully vegetated surface ($\Gamma_c = 0.05$) and bare soil ($\Gamma_s = 0.315$) are empirical constants in equation 2.9. A linear interpolation is performed (as a function of fractional vegetation cover) to get values of soil heat flux. Since net radiation and fractional cover can be estimated from remote sensing data, equation 2.9 becomes feasible to apply on regional or continental scale.

2.4. Sensible heat flux

Sensible heat flux is part of the solar energy consumed by rising warm air from the land surface. Similarity theory and Monin-Obukhov stability correction is applied to calculate the sensible heat flux in the model. The governing equation for mean wind and temperature profiles (in vertical direction) can be written as follows:

$$u = \frac{u^*}{k}\left[ln\left(\frac{z-d_0}{z_{om}}\right) - \psi_m\left(\frac{z-d_0}{L}\right) + \psi_m\left(\frac{z_{om}}{L}\right)\right] \tag{2.10}$$

$$\theta_0 - \theta_a = \frac{H}{ku^* \rho C_p}\left[\ln\left(\frac{z - d_0}{z_{oh}}\right) - \psi_h\left(\frac{z - d_0}{L}\right) + \psi_h\left(\frac{z_{oh}}{L}\right)\right] \tag{2.11}$$

In above equations u and u^* are wind and friction velocity [m/s], z and d_0 are reference meteorological height [m] and displacement height [m] respectively ρ is air density [kg m^{-3}], C_p is heat capacity of dry air [J kg^{-1}], k is von Karman's constant (0.4), z_{om} and z_{oh} are the roughness height for momentum and heat transfer respectively [m]. θ_0 and θ_a are potential temperature at the surface and potential air temperature at height z [K], ψ_m and ψ_h are the stability correction functions for momentum and sensible heat transfer respectively, L is the Obukhov length [m] which is defined as

$$L = -\frac{\rho C_p u^{*3} \theta_v}{kgH} \tag{2.12}$$

In equation 2.12, θ_v is the virtual temperature near the surface [K] and g is the acceleration due to gravity [m s^{-2}].

2.5. Roughness length for heat and momentum transfer

The roughness length for momentum (z_{om}) and heat (z_{oh}) transfer is required to be estimated in order to estimate sensible heat flux. SEBS uses the kB^{-1} model to estimate z_{oh} from z_{om} Su (2002). z_{om} can be estimated from various methods (more details in methodology section). Su (2002) has estimated surface roughness length parameters using Massman model and showed that it can produce reliable estimates for low vegetated areas. The relationship between z_{om} and z_{oh} (according to kB^{-1}) model can be written as

$$z_{oh} = \frac{z_{om}}{exp\left(kB^{-1}\right)} \tag{2.13}$$

In this equation, kB^{-1} is the inverse Stanton number. It is a heat transfer coefficient without dimensions. Su and Jacobs (2001) have further extended the model to estimate the value of kB^{-1}.

$$kB^{-1} = \frac{kC_d}{4C_t \frac{u^*}{u(h)}(1 - e^{-n_{ec}/2})} f_c^{\,2} + 2f_c f_s \frac{k.\frac{u^*}{u(h)}.(z_{om}/h)}{C_t^*} + kB_s^{-1} f_s^2 \tag{2.14}$$

In equation 2.14, f_c and f_s are fractional vegetation cover and its complement respectively, C_t is the heat transfer coefficient of the leaf. Su and Jacobs (2001) suggested that for most canopies and environmental conditions, the C_t value is between $0.005\text{N} \le C_t \le 0.075\text{N}$ (where N is number of sides of a leaf to participate in heat exchange) , The heat transfer coefficient of the soil can be written as $C_t^* = P_r^{-2/3} / R_e^{*-1/2}$, where P_r is the Prandt number. The roughness Reynolds number for soil can be estimated as $R_e^* = h_s u^* / \nu$, where h_s is the roughness height of the soil and v is kinematic viscosity of the air ($\nu = 1.327.10^{-5}.(p_0 / p).(T / T_0)^{1.81}$ where p, T are the ambient pressure and temperature and $p_0 = 101.3$ kPa and $T_0 = 273.15$ K. For bare soil, kB_s^{-1} can be calculated as

$$kB_s^{-1} = 2.46(R_e^*)^{1/4} - \ln[7.4] \tag{2.15}$$

2.6. Evaporative fraction and actual evapotranspiration

The SEBS model estimates evaporative fraction by taking dry and wet limits of sensible heat flux. Since latent heat flux reaches a minimum under dry conditions, it can be neglected in equation 1.1 and surface energy balance closure can be written as $H_{dry} = R_n - G_0$. The wet limit of H can be estimated as follows:

$$H_{wet} = (R_n - G_0) - \left(\frac{\rho C_p}{r_{ew}}\right).\left(\frac{e_s - e}{\gamma}\right) / \left(1 + \frac{\Delta}{\gamma}\right) \tag{2.16}$$

where e and e_s are actual and saturation vapour pressure respectively [hPa]; γ is the psychometric constant [hPaK^{-1}], and Δ is the rate of change of saturation vapour pressure with temperature [hPaK^{-1}]. The aerodynamic resistance at wet limit (r_{ew}) can be calculated as

$$r_{ew} = \frac{1}{ku^*}\left[\ln\left(\frac{z - d_0}{z_{oh}}\right) - \psi_h\left(\frac{z - d_0}{L_w}\right) + \psi_h\left(\frac{z_{oh}}{L_w}\right)\right] \tag{2.17}$$

Similarly, the wet limit stability length can be determined as

$$L_w = -\left[\rho u^{*3} / (kg.0.61.(R_n - G_0)/\lambda)\right] \tag{2.18}$$

Afterwards, relative evaporative fraction (Λ_r) and finally evaporative fraction (Λ) can be calculated as follows (for details Su, 2002).

$$\Lambda_r = \frac{H - H_{wet}}{H_{dry} - H_{wet}}, \quad \Lambda = \frac{\lambda E}{R_n - G_0} = \frac{\Lambda_r - \lambda E_{wet}}{R_n - G_0} \tag{2.19}$$

Once the evaporative fraction is known, the daily mean evapotranspiration can be calculated as

$$\overline{E}_{daily} = 8.64 \times 10^7 \times \overset{24}{\underset{0}{\Lambda}} \times \frac{\overline{R}_n - \overline{G}_0}{\lambda \rho_w} \tag{2.20}$$

In equation 2.20, E_{daily} is daily mean actual evapotranspiration [mm/day], ρ_w is density of water [kg/m^3], and $\overset{24}{\underset{0}{\Lambda}}$ is daily average Evaporative Fraction (*EF*). The conservative nature of evaporative fraction for entire day is well established (Crago and Brutsaert, 1996; Crago, 1996; Sugita and Brutsaert, 1991) and therefore, instantaneous *EF* (estimated from SEBS) can be taken as daily average.

3. Study area

3.1. Location

The geographic location of the study area is between 51.871486 to 52.484905 degrees North and 5.255526 to 6.161426 degree East. It is located in the Gelderland province of the Netherlands (Figure 3.1). The area is mostly flat terrain (except some small hills) and elevation may reach 110m above sea level in some areas.

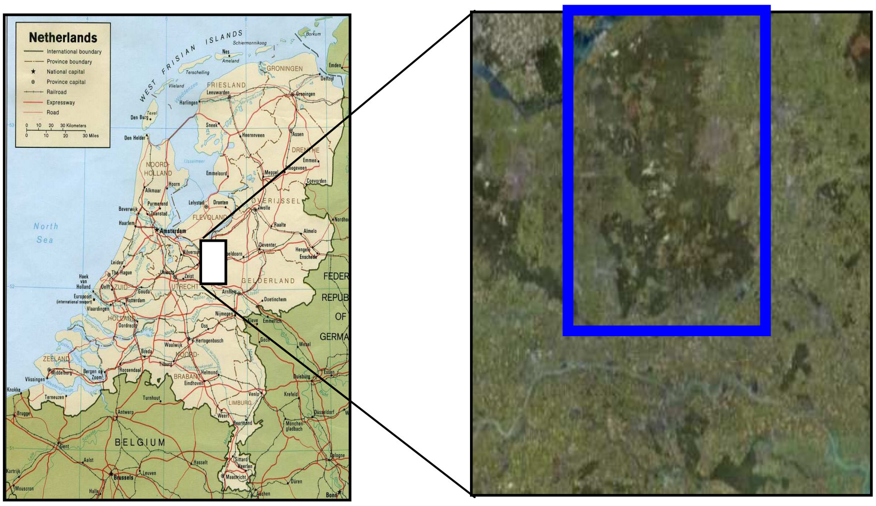

Figure 3.1 Map showing location of the study area (Source: Google earth).

3.2. Climate

The climate in the area is temperate with daytime temperatures ranging from 20 to 25°C in summer and from 0-10°C in winter. Rainfall in the area is fairly steady and takes place throughout the year. The months of April and May are the driest months of the year. The predominant wind direction is south-west. Annual rainfall in the region is 750mm.

3.3. Land cover

The forest consists of coniferous, deciduous and mixed patches. Main landscapes are woodland, heath, small lakes and sand drifts. Major settlements around the area are Arnhem, Apeldoorn, Putten, Ermelo and Wageningen.

4. Materials and instrumentation

4.1. Flux towers

Field measurements of land surface fluxes are required to validate the results obtained from the SEBS and there are three flux measurement sites in the study area. A brief introduction of the sites and height of the measurement is described in following subsections:

- Loobos site

The Loobos site is located near Kootwijk on flat topography in Veluwe forest ridge (52°10'04.286" N, 05°44'38.252" E). It was established in 1994 and is a established Carbo-Europe project site. The maximum flux contribution distance (fetch) is 300m from the tower. The trees in the area are widely spaced and planted on sand dunes. 89% of area around the flux tower consists of Scots pine and 3.5% of the area is open. A number of sophisticated instruments have been installed on the tower for measurement of flux/weather variables at various heights. Table 4.1 shows data description used in the study from the Loobos site.

- Speulderbos site

Another flux monitoring tower is located near Garderen (52°15'08.1"N, 05°41'25.8"E) in Speulderbos forest. The predominant plant species is *Pinus sylvestris* with average tree height of approximately 32 meters. The site is part of Nitro-Europe project and maintained by the National Institute of Public Health and Environment (RIVM). The tower is 47 m high (the highest platform at 46m) and turbulent fluxes are measured at two heights (35m and 47m). The area is slightly undulating and height above mean sea level varies between 10-20m.

- Haarweg site

Haarweg site is a standard agro-meteorological station. It is being operated by the Wageningen University and Research Center. The flux measurement site is located on grassland and surrounded by arable land. The site is located 7m above sea level and the coordinates of the location are 51° 58' N, 5° 38'E.

4.2. Meteorological data

Meteorological observations are ancillary data required in SEBS algorithm. Air temperature, wind speed, pressure and humidity at reference meteorological height were taken as an input in SEBS from Haarweg site as it is a standard weather station.

Table 4.1 Dataset available from three flux towers in the study area.

Variable	**Haarweg site**	**Loobos site**	**Speulderbos site**
Land cover	Grassland	Pine forest	Pine forest
Data availability	Year 2008	Year 2007	Year 2008
Temporal resolution	1 hour	30 min	30 min
Data quality	Processed and gap filled	Processed and flagged	Raw data
Data source	Wageningen University and Research Center	Carbo-Europe flux database	ITC, RIVM, Netherlands
Reference height for wind	10m and 2m	23.5m and 5m	35m and 47m
Incoming shortwave radiation	available	available	available
Soil temperature	10cm, 5cm, 20cm (under grass)	20cm, 30cm, 100cm (under soil)	1, 3, 8, 90 cm (under soil)
Soil heat flux	5cm, (under grass)	10cm (below soil)	10cm (below soil)
Air temperature, pressure and relative humidity	1.5m and 0.1m above ground	23.5m, 7.5m and 5m above ground	35m and 47m above surface
Turbulent fluxes	5m above surface	26m above surface	35m, 47m above surface

4.3. ASTER images

ASTER data are one of the most sophisticated satellite data available with 15 bands ranging from visible to thermal electromagnetic spectrum. In this analysis, ASTER level 2 products (on demand reflectance) have been used. Level 2 products are obtained after geometric and atmospheric correction of level 1A ASTER data. Level 2 ASTER products are distributed by the Land Processes Distributed Active Archive

Centre (LP DAAC). Table 4.2 summarizes obtained level 2 ASTER products. Table 4.3 summarizes acquisition details and data quality of ASTER scenes used in the analysis.

Table 4.2 Description of ASTER data selected acquired in the project.

Bands	**Spectrum range**	**Wavelength (µm)**	**Level 2 product details**
Band 1	Visible 15m resolution	0.52 - 0.60	On demand surface reflectance (AST 07 XT) Projection: UTM Swath: 60km Data format: HDF EOS Valid range: 0-1000 Scale factor: 0.001 Unit: None
Band 2		0.63 - 0.69	
Band 3a	Near infrared 15m resolution	0.76 - 0.86	
Band 3b		0.76 - 0.86	
Band 4	Shortwave 30m resolution	1.60 - 1.70	
Band 5		2.145 - 2.185	
Band 6		2.185 - 2.225	
Band 7		2.235 - 2.285	
Band 8		2.295 - 2.365	
Band 9		2.36 - 2.43	
Band 10	Thermal infrared 90m resolution	8.125 - 8.475	Composite temperature image for all five bands (AST_08) Data: 16 bit unsigned integer Unit: Kelvin Valid range: 200-3200 Scale factor: 0.1
Band 11		8.475 - 8.825	
Band 12		8.925 - 9.275	
Band 13		10.25 - 10.95	
Band 14		10.95 - 11.65	

4.4. Field data collection

Field work was carried out during 1st Oct to 14th Oct. 2008. It was undertaken to accomplish following requirements of the study:

- To estimate fractional vegetation cover in the forest area using digital hemispherical photographs

- Ground Control Points (GCPs) were required for generation of land cover and image registration
- To identify permanent areas of very dense vegetation and bare soil in the study area for calculation of fractional cover from remote sensing image
- To take field spectra of selected land cover types to compare with atmospherically corrected of ASTER images.

Table 4.3 Acquisition details of ASTER scenes.

Acquisition date	**time (GMT)**	**Cloud cover (%)**	**Missing data (%)**	**Interpolated data (%)**
2nd June 2007	10:41am	50	30	30
5th Aug. 2007	10:51 am	0	0	0
27th June 2008	10:57 am	4	25	25
14th Aug. 2008	10:57am	43	4	4
30th Aug. 2008	10:47 am	0	24	24

4.4.1. Sampling design for fractional cover estimate

Stratified random sampling was carried out. In total, sixteen sample points were selected (*Appendix 2 and 4*). Of the identified sampling points, six points were selected in coniferous patches and five points were selected in both deciduous and mixed patches. Initially LICOR 2000 was planned to be used in the entire sampling scheme but due to non-availability of the instrument during the initial days of fieldwork, Digital Hemispherical Photography (DHP) was the only option available. DHP is though widely used method for determination of fractional vegetation cover in forest areas, yet it is subject to uncertainties since it is not a direct measurement of fractional cover (Montes et al., 2008). Zhang et al. (2005) have tried to develop a protocol for taking photographs under the canopy but until now, no standard protocol exist to overcome the uncertainties arising from camera exposure and post image processing.

In order to minimize the uncertainties arising in fractional vegetation cover estimation using DHP, photographs were taken at the maximum possible resolution of 10 megapixels. The advantage of using high resolution is being able to distinguish sky and foliage pixels in the image with more accuracy. A Sigma Fish-eye lens was coupled with Canon EOS 400 digital camera to take photographs. Photographs were taken at three exposure settings (1/250 seconds, 1/800 seconds and 1/1000 seconds) at each sampling point. The stop was kept constant in all the images (F8).

The camera was mounted on tripod and pointed at 90^0 in vertical direction. Azimuth angles of the camera were noted for each photograph which was further used during image registration. The fish-eye lens was kept on autofocus mode to standardize all the samples (avoiding manual focus). No photograph was taken at low battery status of camera. Table 4.4 summarizes the scientific instruments used during field visit.

Table 4.4 Scientific instruments used during field visit.

Instruments	**Purpose**
Garmin GPS	Collection of GCPs
Canon EOS 400 digital camera (10mp)	Digital hemispherical photography of forest canopy
Sigma fish eye lens 8mm,f3.5 auto focus	Digital hemispherical photography of forest canopy
GER Spectroradiometer 3700	Collection of field spectra from various land cover classes
LICOR 2000	Estimation of Leaf Area Index (LAI) and fractional cover

4.4.2. Sampling design for collection of field spectra

Field spectra were also collected for some land cover classes (bare soil, sand, pastures, grassland, heather and top of the forest canopy) using a 1 and 10 degree field of view from GER 3700 Spectroradiometer. Spectra were taken at nadir and 30 degree zenith angles with respect to various azimuth angles. The GER 3700 instrument had measurement errors at channels 1400nm and 2000nm and the reading on both the channel were beyond measurement range. In order to overcome the problem, readings at both channels were removed along with the measurements in the water absorption bands.

Simultaneously, GPS points were also collected for the land cover generation from the satellite image.

5. Methodology

5.1. Pre-processing of ASTER images

Atmospheric correction of the images was not required as images were already corrected for atmospheric attenuation. But a slight positional deviation was observed when two adjacent scenes were compared. Moreover, the surface kinetic temperature product was not georeferenced and it was required to do so for further analysis. ENVI 4.2 and ERDAS 9.1 software were used for pre-processing of the images.

5.2. Estimation of fractional vegetation cover

5.2.1. Fractional vegetation cover from ASTER data

Four methods have been applied (Table 5.1) for fractional cover estimation from ASTER image of 30th Aug. 2008 (15m spatial resolution). The image of 30th Aug. was selected because it was clear day (cloud free) and closest possible time period with respect to field visit (1st to 14th Oct. 2008). The methods NDVI based methods available for fractional vegetation cover estimate from remote sensing data, demand NDVI or surface reflectance values of bare soil and area of infinite LAI (very dense vegetation) in the same image. Both the areas were available in the image and identified during field visit.

Table 5.1 The methods for estimation of fractional cover from ASTER data.

Proposed method	Numerical expression
Method proposed by Baret et al. (1995)	$fc = \left(\frac{NDVI_{\infty} - NDVI_{pixel}}{NDVI_{\infty} - NDVI_{S}} \right)^{K}$
method, proposed by Carlson and Ripley (1997)	$fc = \left(\frac{NDVI_{pixel} - NDVI_{S}}{NDVI_{\infty} - NDVI_{S}} \right)^{2}$
Method proposed by Gutman and Ignatov (1998)	$fc = \left(\frac{NDVI_{pixel} - NDVI_{S}}{NDVI_{\infty} - NDVI_{S}} \right)$
Method proposed by Jiang et.al. (2006)	$fc = \left(\frac{SDVI_{pixel} - SDVI_{S}}{SDVI_{\infty} - SDVI_{S}} \right)$

Where K= 0.6175. $NDVI_{\infty}$ and $NDVI_{S}$ are the NDVI values for vegetation of infinite LAI and bare soil respectively. SDVI is Scaled Difference Vegetation Index (NIR band-Red band). $SDVI_{\infty}$ and $SDVI_{S}$ are the SDVI values for vegetation of infinite LAI and bare soil respectively.

5.2.2. Fractional vegetation cover from hemispherical photographs

The post-processing of hemispherical photographs was carried out using Gap Light Analyser (GLA) software. The software is developed by Institute of Ecosystem Studies in the USA. It calculates the percentage canopy openness by classifying foliage and sky pixels in the image. GLA has been used in a number of such applications with satisfactory results (Frazer et al., 2001; Hardy et al., 2004; Morsdorf et al., 2006; Vacchiano et al., 2006).

Image registration is required in GLA prior to its classification and analysis. The photographs were registered as per azimuth angle information collected during field visit (Chapter 4, section 4.4.1). A threshold has to be decided for each image after registration. The threshold is a pixel brightness value between 0-255 and used by the software to distinguish sky and foliage pixels. The threshold can be defined manually for each image or GLA can define it automatically. In this study, GLA was kept on auto mode. The reason for choosing the automatic threshold was to avoid human error and standardize the analysis for each photograph. The photographs were analyzed in the blue band to reduce mixed pixels in the classification.

The estimates of fractional cover from hemispherical photographs and satellite image were compared. The closest satellite based method with field estimates was used for fractional vegetation cover estimate in SEBS model.

5.2.3. Validation of fractional vegetation cover

The fractional vegetation cover obtained from remote sensing data (for above-mentioned methods) was validated individually with field estimates obtained from digital hemispherical photographs. The paired *t* test was applied taking the difference of each method with field estimates. The population mean was assumed to be zero as in the ideal case mean of the differences between the two methods should be zero (if both are giving identical results). This assumption was the null hypothesis.

$H_o \Rightarrow X_i - X_{field} = 0$ (where $\mu = 0$ and level of significance 95%)

$H_1 \Rightarrow X_i - X_{field} \neq 0$ (X_i fractional cover estimated from remote sensing data and X_{field} is field estimates of the same)

The *t* statistics computed for above hypothesis is $t = \frac{\overline{X} - \mu}{S / \sqrt{n}}$ (where $\overline{X}$ is the mean of difference between fractional cover obtained from methods based on satellite data and field estimates, *S* is standard deviation of the difference and *n* is number of the samples). In other words, if the value of $\overline{X}$ is zero or the lower and upper limit of it includes zero, the method becomes significantly close to field estimates. The upper and lower limits of $\overline{X}$ were calculated from t-statistics.

5.3. Estimation of Leaf Area Index

Leaf Area Index (LAI) is a crucial input parameter in SEBS. By definition, it is total one sided leaf area per unit ground area and considered as representative of upright vegetation. A number of methods have been developed for LAI estimation. Peng et al. (2003) compared twelve different vegetation indices (ranging from visible band to shortwave infrared bands) with LAI and found that Modified Non Linear vegetation Index (MLNI), Simple Ratio (SR), and NDVI correlates best with LAI. In this study, LAI was calculated using method proposed by Su and Jacobs (2001). This method is restricted to low vegetation but this limitation was neglected as none of equation clearly exist for estimation of LAI in forest environments. The numerical expression of the method proposed by Su and Jacobs (2001) is shown in equation 5.1.

$$LAI = NDVI.\left(\frac{1-NDVI}{1+NDVI}\right)^{1/2} \tag{5.1}$$

5.4. Surface emissivity

Surface emissivity is one of the on demand products of ASTER. It is estimated by the Temperature and Emissivity Separation (TES) algorithm. The surface emissivity product of ASTER was directly used in the model.

5.5. Roughness length for momentum transfer (z_{om})

Estimation of z_{om} is very crucial for surface energy balance modelling (Su, 2002). It is very difficult to find the correct values for z_{om} as it requires extensive data of vertical wind profiles. In remote sensing based surface energy balance models, it is defined as a function of either NDVI or LAI (Su, 2005). The two methods (based on vegetation index) for derivation of z_{om} from NDVI are described in equation 5.2 and 5.3 (Su and Jacobs, 2001).

$$z_{om} = 0.005 + 0.5 \times \left(\frac{NDVI}{NDVI_{\max}}\right)^{2.5} \tag{5.2}$$

$$z_{om} = \exp(-5.2 + 5.3 \times NDVI) \tag{5.3}$$

Previous research suggests that both the methods give similar values for the z_{om} below NDVI values of 0.7. But for higher NDVI values (~1), equation 5.3 gives the z_{om} values greater than 1.0m (Su and Jacobs, 2001). The z_{om} can also be estimated from the literature by assigning roughness length for each land cover class (Reithmaier et al., 2006). Table 5.2 shows the z_{om} values proposed by various scientists on the basis of land cover. In this study, the z_{om} values were derived from equation 5.2 which is default method in SEBS code. The vegetation height (*h*) and zero plane displacement height (*d*) were estimated from the method proposed by Brutsaert (1982).

$$h = \frac{z_{om}}{0.136} \qquad d = \frac{2}{3} h \tag{5.4}$$

In equation 5.4, both *h* and *d* are in meters.

Table 5.2 z_{om} values assigned on the land cover basis (Reithmaier et al., 2006).

Land cover	z_{om} Value [m]			
	Davenport, 2000	**Hasager and Jensen, 1999**	**Wieringa, 1992**	**Toren and Peterson, 1989**
Conifer	1.0	0.9	1.6	0.4
Deciduous	2.0	1.2	1.7	0.4
Clearings	0.2	0.004	0.35	0.1
Shrubs	0.5	0.3	0.45	0.4
Grasslands	0.03	0.08	0.06	0.03
Summer crops	0.25	0.09	0.18	0.1
Winter crops	0.1	0.12	0.09	0.1
Bare soil	0.005	0.03	0.004	0.03
Settlement	2.0	0.5	0.7	0.4
Quarry	0.2	0.004	0.35	0.1
Unclassified	0	0	0	0

5.6. Sensitivity analysis of the model

Sensitivity analysis evaluates the sensitivity of a model output to the range of defined variation of an input parameter (Salehi et al., 2000). It does not focus on the variation in the output due to the variance in the inputs, but can assess the change in the model output by range of variations in the input values (Bolger, 1996). This process helps in indentifying the input variables for which high certainty is required in measurement/estimation and also the variables.

Sensitivity analysis has been carried out for the SEBS model for input parameters derived from ASTER data (NDVI, fractional vegetation cover, land surface temperature, surface albedo and emissivity). The sensitivity analysis was conducted using Independent Parameter Perturbation (Chaves and Nearing, 1991; Ik-Jae Kim et al., 2007). The sensitivity of the model can be calculated using equation 5.5.

$$S = \frac{O_i - O_G}{O_G} \times 100 \qquad (5.5)$$

In equation 5.5, O_i is model output after changing the independent input parameter, and O_G is the model output for the base value. The output response of SEBS was calculated from -50% to +50% of the base value for each input parameter derived from ASTER data. Model output responses were calculated in terms of fixed percentage change of each input parameter. Each input parameter was varied from −50 to +50% in 10 intervals (−50, −40, −30, −20, −10, +10, +20, +30, +40, +50) for the base value (base value is 0% change). The range of perturbation becomes ±50% for each input variable making the process uniform.

6. Results and discussion

6.1. Evaluation of ASTER data

The atmospheric correction of the image was compared with field spectra collected during field visit. Figure 6.1 shows the comparison of atmospherically corrected ASTER image data with field spectra for sand and pasture (resampled to ASTER spectral resolution).

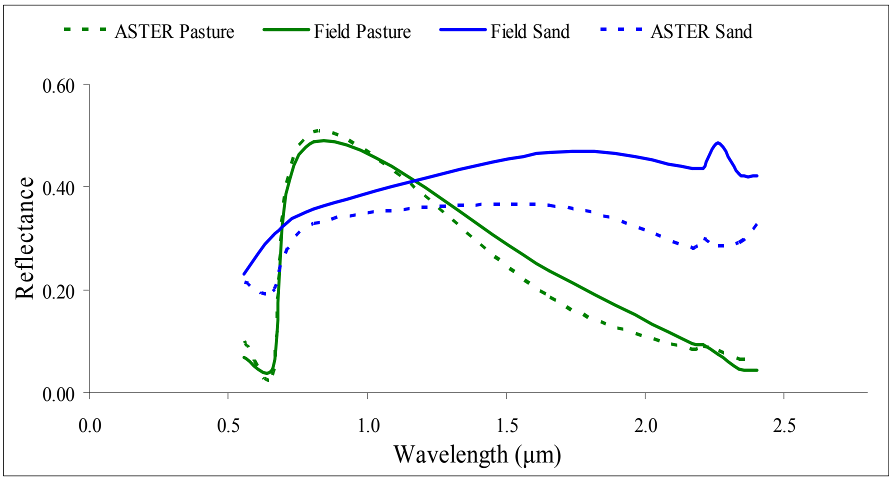

Figure 6.1 Comparison of ASTER bands with collected field spectra.

The comparison shows a good quality of atmospheric correction. It brings confidence in the image data for further analysis. However, at 0.6µm, typical vegetation absorption pattern was observed in sand pixel of ASTER image. It is a common problem in remote sensing data due to adjacency effects and may remain in some pixels even after atmospheric correction (Zhu and Bettinger, 2008). Otherwise, the overall pattern of the satellite data is showing similar trend with field spectra for sand and vegetation.

6.2. Fractional vegetation cover

The estimates of fractional cover obtained from hemispherical photographs were compared with estimates obtained from (remote sensing data methods). It has been found that the method proposed by Gutman and Ignatov (1998) performs the best amongst the methods applied. Figure 6.2 to 6.6 show the upper limit, lower limit and the difference in the mean of each method with respect to field data. A two tailed paired *t*-test was carried out assuming population mean to be zero (Chapter 5, section 5.2.3).

The results shown in Figure 6.2 were calculated on all the 16 samples collected in the field. Though none of the methods is significantly close to field data (α = 0.05) yet the method proposed by Gutman and Ignatov has the closest values with low variance. The method proposed by Jiang et al. (2006) is far away from field estimates. The reason for such deviation can be explained from its formulation as the method is based on Scaled Difference Vegetation Index (SDVI). SDVI is sensitive to atmospheric attenuation. In contrast, the other three methods are based on NDVI approach (Table 5.1). Since NDVI is least sensitive to atmospheric attenuation, these methods are less sensitive to slight change in surface reflectance.

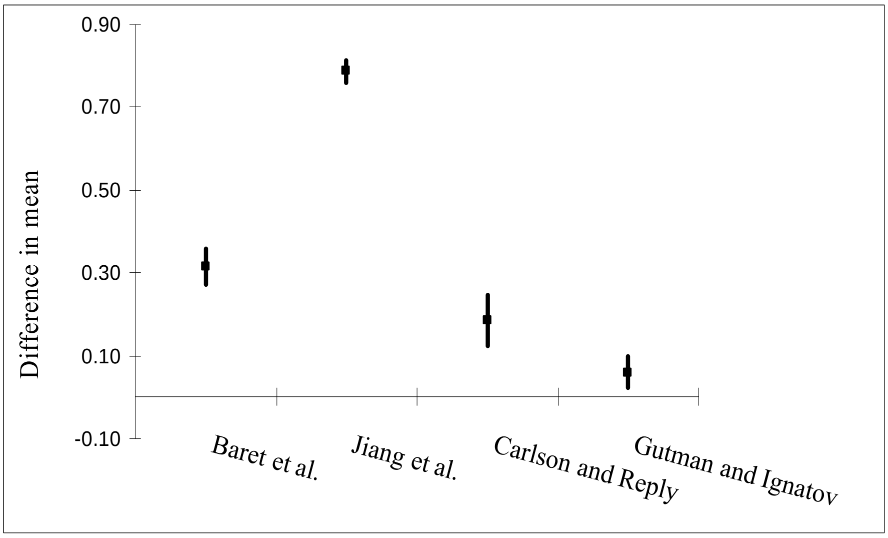

Figure 6.2 The difference in the mean (between field estimates and satellite based methods) for fractional cover estimates (all 16 samples).

A sensitivity analysis of all the four methods was carried out to prove above-mentioned explanation for the method of Jiang et al. (2006). Sensitivity analysis supports the evidence (Figure 6.3) that the Jiang et al. method is more sensitive to slight change in surface reflectance. On the other hand, the Gutman and Ignatov method is least sensitive to this.

The forest patches were also compared separately (broad leaf, coniferous and mixed patches) with field estimates. The method proposed by Gutman and Ignatov shows significance (α = 0.05) in both broad leaf and mixed forest class. Maximum significance was found in the broad leaf class. On the other hand, none of the methods were close to field data except the Gutman and Ignatov method for coniferous forest patch.

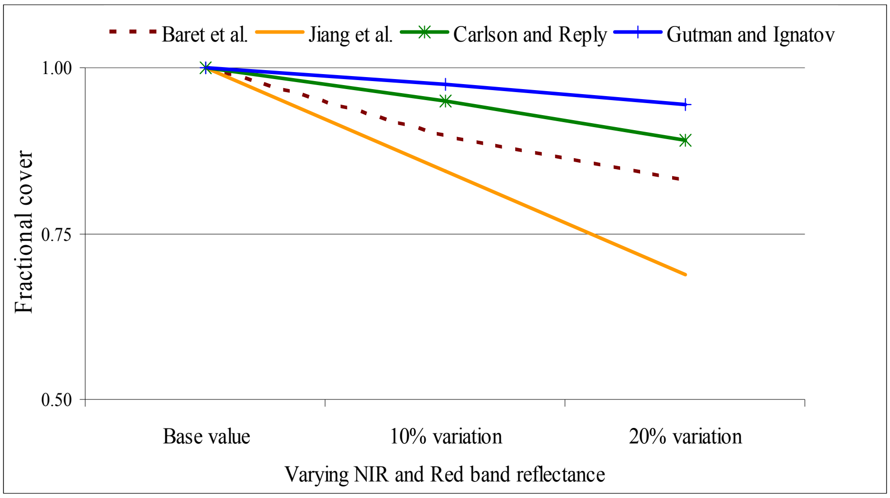

Figure 6.3 Sensitivity analysis performed on all the four approaches for fractional cover estimation from satellite data.

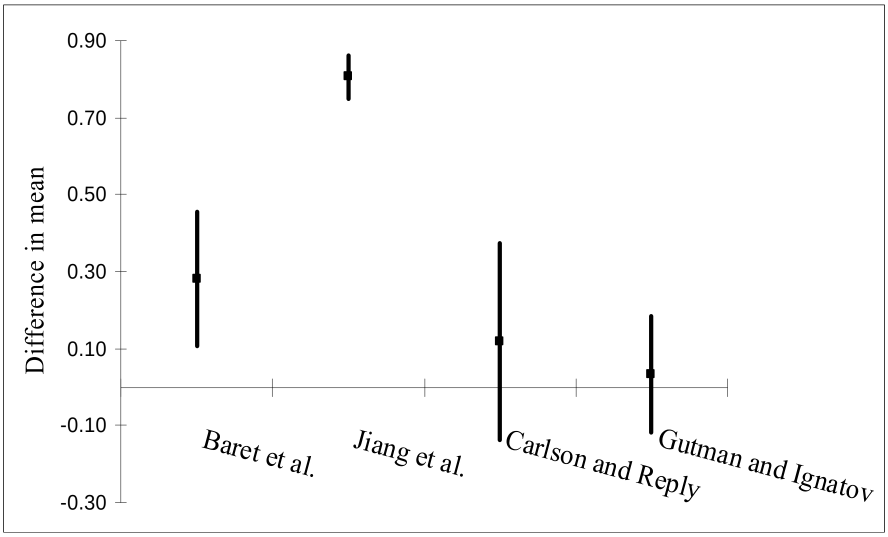

Figure 6.4 The difference in the mean (between satellite data based methods) and field estimates for fractional cover estimates (broad leaf forest patch)

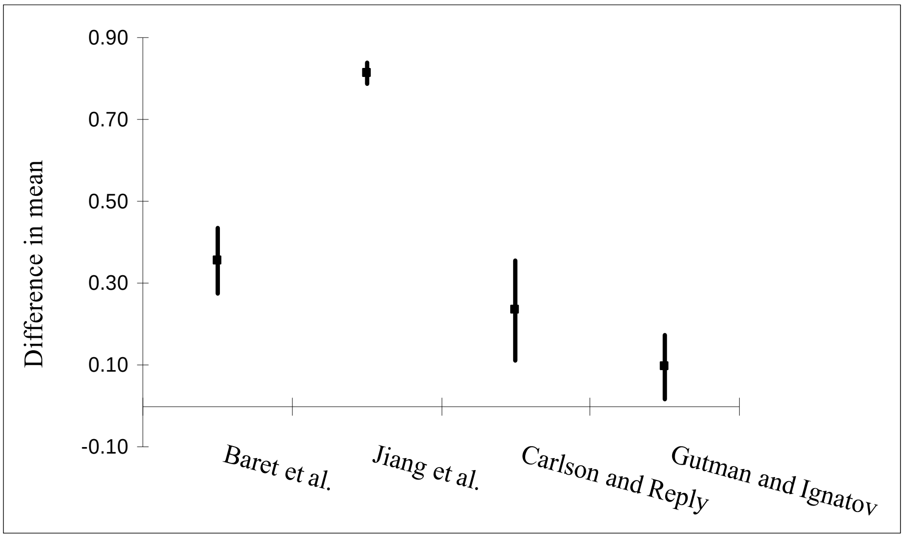

Figure 6.5 The difference in the mean (between satellite data based methods) and field estimates for fractional cover estimates (coniferous forest patch).

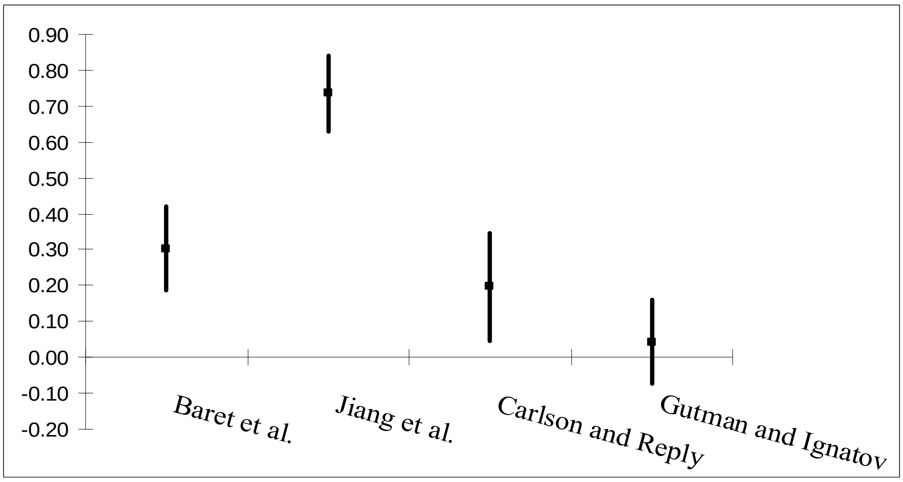

Figure 6.6 The difference in the mean (between satellite data based methods) and field estimates for fractional cover estimates (mixed forest patch).

The non-significance of remote sensing based methods for fractional cover estimates can be explained from clumping effect of coniferous forests (Garrigues et al., 2008; Montes et al., 2007; Morsdorf et al., 2006). Still the method proposed by Gutman and Ignatov performs the best in all types of circumstances and used for further analysis.

6.3. Diurnal behaviour of turbulent fluxes

Figure 6.7 shows diurnal behavior of the surface energy balance closure. Compared to turbulent fluxes (sensible heat and latent heat), soil heat flux can be considered negligible in dense canopies. As shown in Figure 6.7 turbulent fluxes starts increasing with net radiation and reaches their peak value during mid day. The variation in net radiation is very smooth. On the other hand, sensible and latent heat fluxes are very unstable throughout the day and difficult to estimate from one single remote sensing image as it can either underestimate or overestimate the daily average value. Besides, even for instantaneous values of turbulent fluxes, it is difficult to say what temporal resolution (one minute/hour or second) can be represented by a remote sensing image.

Though soil heat flux is negligible, it exponentially increases from negative values to its peak value during mid day. It is obvious from Figure 6.8 that the entire process of surface energy balance closure is time dependent and depends on local solar time. In order to estimate daily average values of sensible and latent heat flux, at least minimum and maximum values are required which can be estimated by taking satellite images during night time (when turbulent fluxes are at minimum) and at noon (when turbulent fluxes are at maximum). Figure 6.8 shows measured parameters of the surface energy balance closure for the Haarweg site (5th Aug. 2007). There is a significant difference in net radiation in both the sites (225.5 W/m^2 diurnal mean for the Loobos site and 141.8W/m^2 for Haarweg site). The high value of soil heat flux at the Haarweg site (compared to the Loobos site) can be explained by its land cover as it is a agro-meteorological station and does not have high canopies like the Loobos forest site.

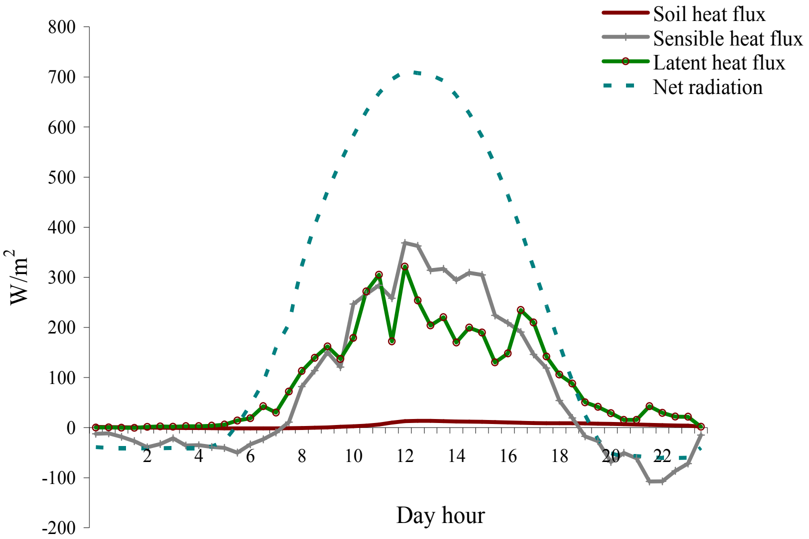

Figure 6.7 Diurnal behaviour of surface energy fluxes on 5th Aug. 2007 at Loobos site.

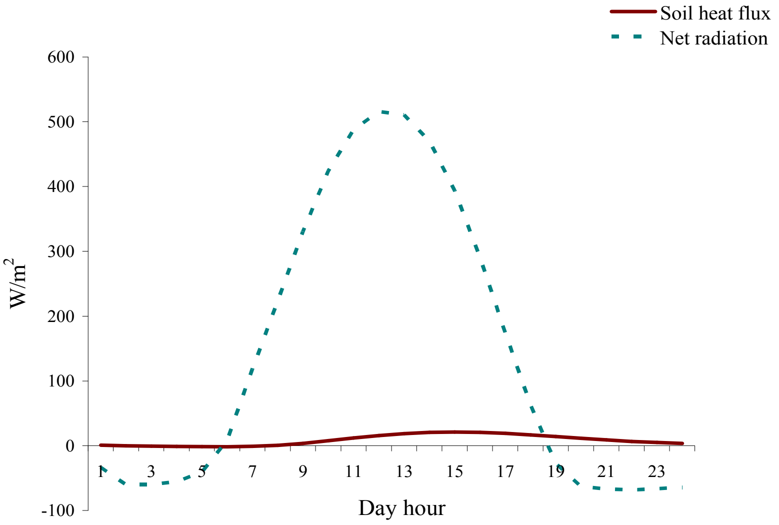

Figure 6.8 Diurnal behaviour of energy fluxes on 5th Aug. 2007 at Haarweg site.

6.4. Measured vs. estimated soil heat flux

Table 6.1 shows the measured versus estimated values of soil heat flux from both the methods (Su, 2002; Bastiaanssen et al., 1998). The Root Mean Square Error (RMSE) was also calculated. It is clear from Table 6.1 that both the methods are overestimating the soil heat flux. The estimated values are in the range of 30-40 W/m^2 compared to measured values (1-12 W/m^2). Result shows that the method proposed by Bastiaanssen et al. (1998) has a smaller RMSE value. It was also confirmed by Verstraeten et al., (2005) in their study by comparing estimated soil heat flux with Carbo-Europe flux net data.

Table 6.1 Measured versus estimated soil heat flux (W/m^2).

Site Name	*G* Measured	G_1	G_2	*G* Daily (measured avg.)
Loobos	10	35	36	5
Loobos	9	39	58	4
Haarweg	12	37	36	8
Haarweg	12	32	32	8
Speulderbos	2	31	36	8
Speulderbos	-1	33	45	5
RMSE		27.5	35.3	

G_1-Mehtod proposed by Bastiaanssen et al. (1998),
G_2-Method proposed by Su (2002).

Both approaches developed for soil heat flux are based on NDVI (Su, 2002) and some coefficients (Bastiaanssen et al., 1998). Verstraeten et al, (2005) suggest that a saturation effect of NDVI or inappropriate coefficients may lead to overestimation of soil heat flux which is possibly explaining canopy heat storage indirectly. Secondly, the measured values of soil heat flux in forest areas are very low compared to other surface energy closure terms (Table 6.1 and 6.2). Therefore, the question arises if there should be two different models at regional scale for low vegetated areas (taking *G* into account) and high canopies (ignoring *G*) for estimation of surface energy fluxes as overestimation of one fraction of R_n can lead to underestimation of another.

6.5. Measured vs. estimated turbulent fluxes

Table 6.2 shows measured versus estimated turbulent fluxes (latent and sensible heat). The RMSE of the estimation of sensible heat and latent heat flux is very high (>50 W/m^2). Besides, there is underestimation of sensible heat and overestimation of latent heat flux.

The estimated values match neither with measured instantaneous nor with daily average values. It is as per expected as both sensible and latent heat are very unstable (Figure 6.7) throughout the day. Besides, it has also been proven that estimation of aerodynamic surface length is a major weakness and at present, none of the methods is good enough to estimate aerodynamic roughness length from remote sensing data (Su, 2002). The method used to estimate the roughness length of momentum and heat transfers has underestimated the z_{om} values for the forest area (Table 6.3).

Table 6.2 Measured and estimated turbulent fluxes (W/m^2).

Site	**Estimated**		**Measured (instantaneous)**		**Day average (measured)**	
	H	***LE***	***H***	***LE***	***H***	***LE***
Loobos	81	440	258	172	78	95
Loobos	27	327	348	206	80	68
Speulderbos	40	309	75	47	12	14
Speulderbos	61	259	180	142	23	53
Speulderbos	108	304	394	169	82	113

Table 6.3 Estimated vegetation parameters for validation pixels in forest

Parameter	**1 LB**	**2 LB**	**3 LB**	**1 SB**	**2 SB**	**3 SB**
z_{om} (m)	0.32	0.30	1.70	0.40	0.44	1.70
Vegetation height (m)	2.37	2.26	12.50	2.94	3.26	12.50
Displacement height (m)	1.58	1.50	8.33	1.96	2.17	8.33

In Table 6.3, z_{om} values for the Loobos and the Speulderbos site were estimated from three different methods (1 is the method proposed by Su and Jacobs, 2001; 2 is the method proposed by Bastiaanssen, 1995 and 3 is the z_{om} value taken from the literature, Table 5.2). LB and SB stands for Loobos and Speulderbos site respectively.

Table 6.3 shows that none of the proposed methods is good enough to represent the z_{om} and vegetation height values for both the forest sites (as the vegetation height is 32m for Speulderbos and ~20m for Loobos site). Though the z_{om} value taken from literature can represent forest area to some extent but it is half of the actual values. The other two methods are not suitable for forest area. The lower values of H estimated from SEBS (using Su and Jacobs method) explain underestimation of sensible heat as it is directly proportional to z_{om}. Since one fraction of R_n has been underestimated (H), other fraction of R_n (LE) has been overestimated.

6.6. Measured vs. estimated evaporative fraction (*EF*)

Table 6.4 shows the estimated (from SEBS) and calculated values (from flux measurements) of evaporative fraction. As expected from results of sensible and latent heat flux, overestimation of the latent heat flux led to higher values of the evaporative fraction (RMSE 0.47) for forest land cover (for both instantaneous and daily average values of measured data).

Table 6.4 Measured and estimated values of Evaporative Fraction (*EF*).

Site	**Evaporative fraction**		
	Measured	**Estimated (SEBS)**	**Daily average (measured)**
Loobos	0.40	0.85	0.55
Loobos	0.37	0.92	0.46
Speulderbos	0.38	0.89	0.54
Speulderbos	0.44	0.81	0.70
Speulderbos	0.30	0.74	0.58
RMSE (instantaneous)	0.47		
RMSE (daily average)	0.55		

RMSE values of a similar range (0.19-0.42) were also mentioned by Verstraeten et al. (2005) in their study for the Loobos site. In this study, the image resolution does not seem to have impact on the results of evaporative fraction. The study carried out by Verstraeten et al. (2005) was conducted on NOAA imagery of 1.1km pixel size compared to this study carried out at 90m spatial resolution. The negligence of image resolution might have happened due to mismatch of eddy covariance fetch (~300m) and image pixel size (Li et al., 2008). But Li et al. (2008) have reported significant impact of image resolution (1.0km versus 120-30m) on RMSE values of all the fluxes using two source model. Another possibility is that errors in estimation of *H* and *LE* have (due to aerodynamic roughness length) dominated the positive effects of high image resolution.

6.7. Sensitivity analysis

The procedure carried out for sensitivity analysis is explained in methodology section. The sensitivity of the SEBS output (*EF*, R_n, *LE* and *H*) are explained below for satellite inputs used in SEBS.

6.7.1. Surface albedo

In Figure 6.9 the variations in SEBS output with respect to albedo are shown. As expected, surface albedo directly affects the net radiation. SEBS uses net radiation to calculate soil heat flux and because of that, soil heat flux also changes with same rate. But the cumulative impact of R_n and *G* increases the sensitivity of *LE* to Albedo. Since sensible heat flux is not affected by albedo, the variation in evaporative fraction is small compared to the other three variables.

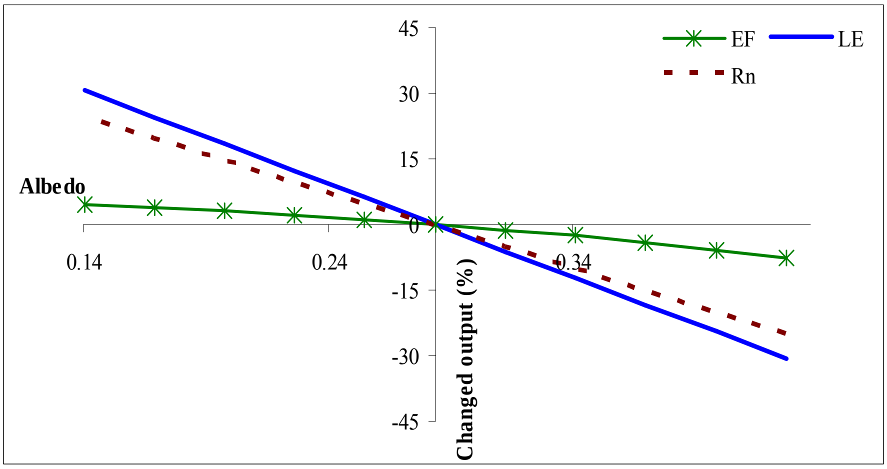

Figure 6.9 Sensitivity of SEBS with respect to surface albedo.

6.7.2. Surface emissivity

Figure 6.10 shows the variations in SEBS output with respect to surface emissivity. Like albedo, emissivity is also related to R_n which causes changes in R_n, *G* and *LE* but not in *H*. Due to this, the variations in *EF* are very smooth throughout the range of plausible emissivity values.

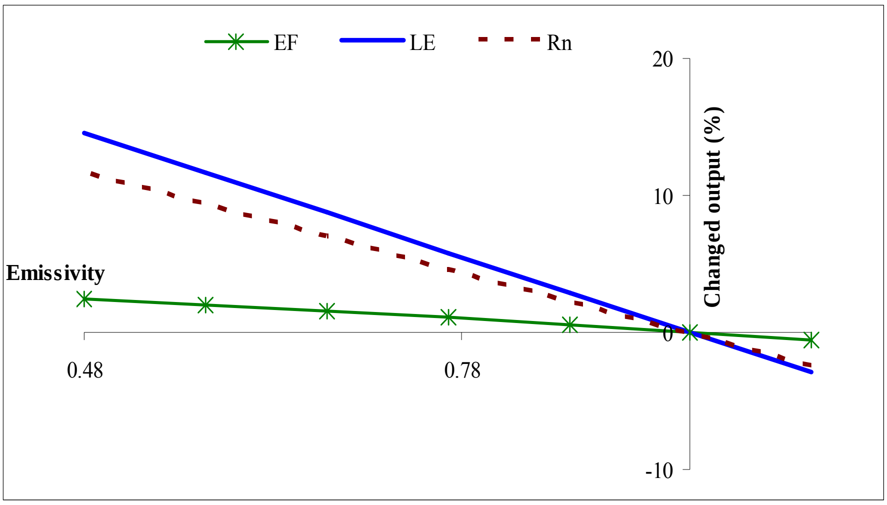

Figure 6.10 Sensitivity of SEBS with respect to surface emissivity.

6.7.3. Land surface temperature (LST)

The variations in SEBS outputs with respect to LST are shown in Figure 6.11. Apparently, LST is the most crucial remote sensing data input in SEBS as it changes almost every parameter. Besides, the impact on *H*, *LE* and *EF* are high compared to the other input parameters. Since sensible heat flux is a function of LST, the sensible heat flux increases exponentially after 30-32^{0}C LST values. This results in high negative changes of *LE* and *EF*. Between 20-30^{0}C LST values, *H* becomes negative, resulting in a positive variation in *LE* and *EF*.

6.7.4. Fractional vegetation cover

Figure 6.12 explains the sensitivity of SEBS output with respect to fractional vegetation cover. It is important to note that *H* is very much dependent on fractional cover as Massman's model (equation 2.14) is used in SEBS to estimate surface roughness length for heat transfer (z_{oh}). In this model of Massman (Chapter 2, section 2.5) both fractional cover and compliment of it have been parameterized for estimation of z_{oh}. Sensitivity of SEBS with respect to fractional vegetation cover shows that it is the second most important input variable (after LST) derived from remote sensing data. It has a significant impact on *H* and *EF*. There are a number of empirical approaches available to estimate fractional cover from remote sensing images and therefore, utmost care should be taken to choose the method that fits best to the field conditions.

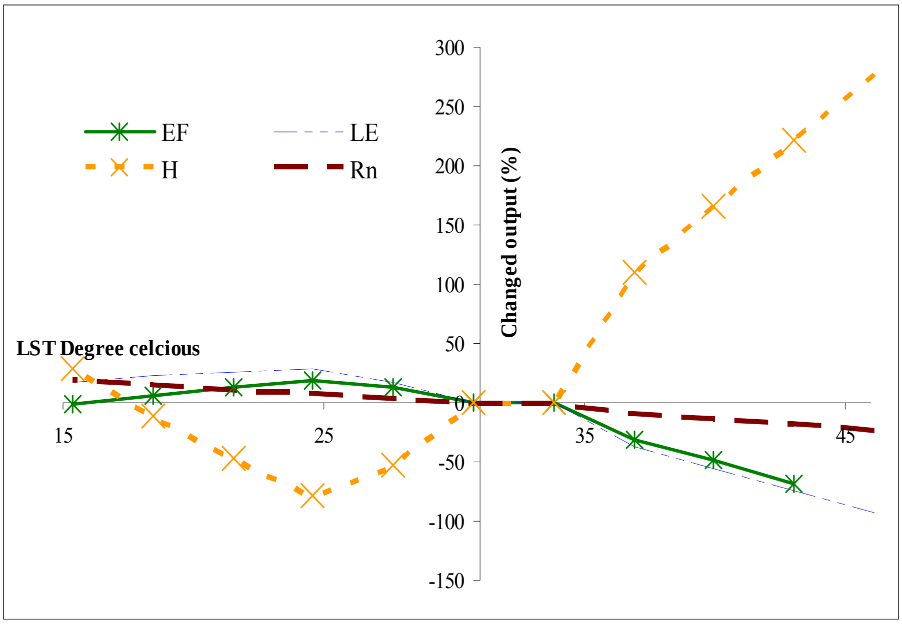

Figure 6.11 Sensitivity of SEBS with respect to land surface temperature (LST).

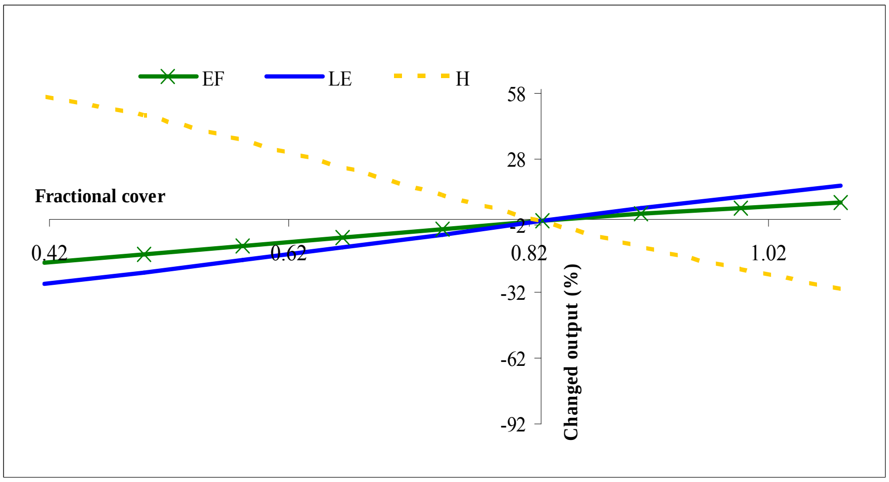

Figure 6.12 Sensitivity of SEBS with respect to fractional vegetation cover (The value1.02 on x axis is theoretical and practically not possible).

6.7.5. NDVI

The SEBS model uses NDVI values in two ways. First is to estimate fractional vegetation cover. The second one is to estimate kB^{-1} term (equation 2.14) and LAI. The Figure 6.13 shows the sensitivity of SEBS output with respect to NDVI for the latter case as fractional vegetation cover is separately discussed (section 6.7.4). Sensitivity analysis shows that SEBS outputs do not change beyond NDVI value of 0.55. On the other hand, there is variation of 0 to 16% in sensible heat at NDVI values ranging from 0.39 to 0.55. Similarly, the evaporative fraction and latent heat are also varying up to 4% at NDVI values ranging from 0.39 to 0.55.

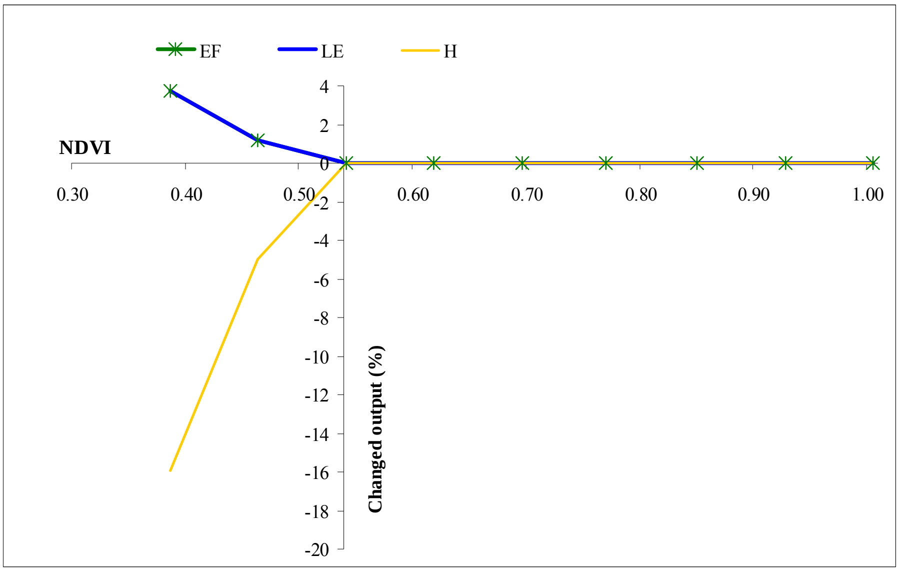

Figure 6.13 Sensitivity of SEBS with respect to NDVI.

Therefore, it can be concluded that SEBS output is more sensitive to lower NDVI values than higher NDVI. Apparently, there is no impact of increasing NDVI values (beyond 0.55) on SEBS output but, it is expected to vary (since z_{om} and LAI are based on NDVI in the model). Further investigation of this behaviour of SEBS with respect to NDVI was not carried out as it was beyond the scope of this research.

7. Conclusions and recommandations

7.1. Conclusions

The principle of surface energy balance closure applied in SEBS is a useful technique to estimate surface energy fluxes. At the same time, due to the large variations in diurnal cycles of turbulent fluxes, instantaneous or daily average sensible and latent heat fluxes are difficult to obtain from remote sensing data. Besides, none of the remote sensing based model could represent aerodynamic roughness length parameters (z_{om}, d and h) accurately for forest land cover (Table 6.3). Estimation of biophysical parameters from remote sensing data is a crucial step and requires utmost care as SEBS output varies with them. The following are the specific conclusions related to the research questions raised in the study:

1. Which method of fractional vegetation cover estimation (from remote sensing data) is close to field estimates?

Out of the four methods tested for fractional vegetation cover estimation, the method proposed by Gutman and Ignatov (1998) matches best with the filed estimates from digital hemispherical photographs.

2. Which empirical relationship (Su, 2002; Bastiaanssen et al., 1998) leads to better estimates of soil heat flux?

Both methods overestimate soil heat flux and none of them is close to measured values. However, the method proposed by Bastiaanssen et al., (1998) has lower RMSE (Table 6.1) than the method proposed by Su (2002).

3. Are instantaneous (derived from SEBS) and mean diurnal (field data) evaporative fraction comparable? If not, how much is the deviation from the daily mean of the field data?

Instantaneous and *EF* derived from SEBS and mean diurnal *EF* (derived from measured data) vary with RMSE 0.47 for instantaneous values and RMSE 0.55 for daily average values. The model overestimates latent heat flux and underestimates sensible heat flux (Table 6.2) in forest land cover causing higher than calculated values (from field data) of evaporative fraction.

4. To which remote sensing input parameter, the evaporative fraction (SEBS output) is the most sensitive.

It was found that, out of remote sensing data input (NDVI, fractional vegetation cover, land surface temperature, albedo and emissivity) tested in sensitivity analysis, land surface temperature is the parameter to which SEBS is most sensitive.

7.2. Limitations of the research

- There are limitations in the estimation of sensible heat flux as none of the present model can estimate aerodynamic roughness length for heat and momentum transfer accurately from satellite data (Su, 2002). This particular field has not been touched in this research.
- The method proposed for z_{om} estimation from literature was not applied which may have a crucial role in underestimation of sensible heat flux.
- Sensitivity analysis was carried out on the input data derived from remote sensing images and not on other input variables (meteorological variables, surface roughness length for momentum and heat transfer, displacement height, etc.).
- The short wave channels (6 bands) of ASTER data from April 2008 overestimate surface reflectance. It is a known anomaly of ASTER shortwave data and flagged by ASTER data distribution centre. This anomaly may affect calculation of surface albedo for images of the year 2008.
- Many equations used in the estimation of SEBS are empirical and may vary with field conditions.

7.3. Recommandations

- Soil heat flux in the forest area is negligible compared to other surface energy terms. It should be explicit in models being used for estimation of evapotranspiration on regional scale as it might increase/decrease the accuracy of estimation and it is useful to look into how can soil heat flux be represented for low vegetated areas and high canopies in one model.
- The entire surface energy balance closure is governed by the local solar cycle (local solar time) for each day of the year and it is important to understand what time step satellite data may represent and how it can be extrapolate over entire day.
- Digital Surface Model (DSM) can be helpful in addressing the vegetation height parameter which can give good estimation of aerodynamic

roughness length for momentum and heat transfer. More emphasis should be given to make such data available on regional or global scale.

- A simple model can be developed which may give good results instead of developing complex models. For example, a single variable, namely wind speed measured at standard meteorological station Haarweg (at 10m height) can explain ~70% of the variability in hourly latent heat flux and ~77% of the variably in hourly sensible heat flux measured at Loobos site (*Appendix 1A and 1B*). This correlation can be explained from formulation of aerodynamic resistant where wind speed is taken as an input to equation 2.10 and 2.11.

8. References

Baret, F., Clevers, J.G.P.W. and Steven, M.D., 1995. The robustness of canopy gap fraction estimations from red and near-infrared reflectances: A comparison of approaches. Remote Sensing of Environment, 54: 141-151.

Bastiaanssen, W.G.M., 1995. Regionalization of surface flux densities and moisture indicators in composite terrain: a remote sensing approach under clear skies in mediterranean climates, Landbouwuniversiteit Wageningen, Wageningen, 273 pp.

Bastiaanssen, W.G.M., Menenti, M., Feddes, R. A. and Holtslag, A. A. M., 1998. A remote sensing surface energy balance algorithm for land (SEBAL): Formulation. Journal of Hydrology, 212-213: 198-212.

Betts, A.K. and Beljaars, A.C.M., 1993. Estimation of effective roughness length for heat and momentum from FIFE data. Atmospheric Research, 30: 251-261.

Bolger, F., 1996. Uncertainty: A guide to dealing with uncertainty in quantitative risk and policy analysis - Morgan,MG, Henrion,M. Journal of Behavioral Decision Making, 9(2): 147-148.

Brutsaert, W., 1982. Evaporation into the atmosphere: theory, history, and applications. Copy. Reidel Publishing, Dordrecht, 299 pp.

Campbell, G.S. and Norman, J.M., 1998. Introduction to environmental biophysics. Springer, New York, 286 pp.

Carlson, T.N., and Ripley, D.A., 1997. On the relation between NDVI, fractional vegetation cover and leaf area index. Remote Sensing of Environment, 62: 241-252.

Chaves, H.M.L. and Nearing, M.A., 1991. Uncertainty Analysis of the Wepp Soil-Erosion Model. Transactions of the Asae, 34(6): 2437-2445.

Crago, R. and Brutsaert, W., 1996. Daytime evaporation and the self-preservation of the evaporative fraction and the Bowen ratio. Journal of Hydrology, 178(1-4): 241-255.

Crago, R.D., 1996. Conservation and variability of the evaporative fraction during the daytime. Journal of Hydrology, 180(1-4): 173-194.

Dingman, S.L., 2002. Physical hydrology. Prentice Hall, Upper Saddle River, 646 pp.

Frazer, G.W., Fournier, R.A., Trofymow, J.A. and Hall, R.J., 2001. A comparison of digital and film fisheye photography for analysis of forest canopy structure and gap light transmission. Agricultural and Forest Meteorology, 109(4): 249-263.

French, A.N., Jacob, F., Anderson, M.C., Kustas, W.P., Timmermans, W., Gieske, A., Su, Z., Su, H., McCabe, M.F., Li, F., Prueger, J. and Brunsell, N., 2005. Surface energy fluxes with the Advanced Spaceborne Thermal Emission and Reflection radiometer (ASTER) at the Iowa 2002 SMACEX site (USA). Remote Sensing of Environment, 99(1-2): 55-65.

Garrigues, S., Shabanov, N.V., Swanson, K., Morisette, J.T., Baret, F. and Myneni, R.B., 2008. Intercomparison and sensitivity analysis of Leaf Area Index retrievals from LAI-2000, AccuPAR, and digital hemispherical photography over croplands. Agricultural and Forest Meteorology, 148(8-9): 1193-1209.

Gutman, G. and Ignatov, A., 1998. The derivation of the green vegetation fraction from NOAA/AVHRR data for use in numerical weather prediction models. International Journal of Remote sensing, 19: 1533-1543.

Hall, F.G., 1992. Satellite remote sensing of surface energy balance : success, failures, and unresolved issues in FIFE. Journal of Geophysical Research, 97: 19,061-19,089.

Hardy, J.P., Melloh, R., Koenig, G., Marks, D., Winstral, A., Pomeroy, J.W. and Link, T., 2004. Solar radiation transmission through conifer canopies. Agricultural and Forest Meteorology, 126(3-4): 257-270.

Ik-Jae Kim, S.L., Hutchinson J.M., Shawn H.C. and Bryan Y., 2007. Riparian Ecosystem Management Model: Sensitivity to Soil, Vegetation, and Weather Input Parameters. Journal of the American Water Resources Association, 43(5): 1171-1182.

Jia, L., Su, Z., van den Hurk, B.J.J.M., Menenti, M., Moene, A.R., de Bruin, H.A.R., Baselga Yrisarry, J.J., Ibanez, M. and Cuesta, A., 2003. Estimation of sensible heat flux using the surface energy balance system SEBS and ATSR measurements. Physics and chemistry of the earth, 28(1-3): 75-88.

Jiang, Z., Huete, A.R., Chen, J., Chen, Y., Li, J., Yan, G. and Zhang, X., 2006. Analysis of NDVI and scaled difference vegetation index retrievals of vegetation fraction. Remote Sensing of Environment, 101(3): 366-378.

Liang, S., Shuey, C.J., Russ, A.L., Fang, H., Chen, M., Walthall, C.L., Daughtry, C.S.T and Hunt, R.Jr., 2002. Narrowband to broadband conversions of land surface albedo: II. Validation. Remote Sensing of Environment, 84: 25–41.

Kimura, R., Bai, L., Fan, J., Takayama, N. and Hinokidani, O., 2007. Evapotranspiration estimation over the river basin of the Loess Plateau of China based on remote sensing. Journal of Arid Environments, 68(1): 53-65.

Kustas, W.P., Schmugge, T.J., Humes, K.S., Jackson, T.H., Parry, R. and Weltz, M.A.,, 1993. Relationships between evaporative fraction and remotely sensed vegetation index and microwave brightness temperature for semiarid rangelands. Journal of Applied Meteorology, 32: 1781-1790.

lders, N. and Raabe, A., 1996. Numerical Investigations on the Influence of Subgrid-Scale Surface Heterogeneity on Evapotranspiration and Cloud processes. Journal of Applied Meteorology, 35(6): 782-795.

Li, F., Kustas, W.P., Anderson, M.C., Prueger, J.H. and Scott, R.L., 2008. Effect of remote sensing spatial resolution on interpreting tower-based flux observations. Remote Sensing of Environment, 112(2): 337-349.

Menenti, M. and Choudhury, B.J., 1993. Parameterization of land surface evapotranspiration and surface temperature range. Exchange Process at the Land Surface for the Range of Space and Time Scales. IAHS, 516-568 pp.

Montes, F., Rubio, A., Barbeito, I. and Cañellas, I., 2008. Characterization of the spatial structure of the canopy in Pinus silvestris L. stands in Central Spain from hemispherical photographs. Forest Ecology and Management, 255(3-4): 580-590.

Moran, M.S., Clarke, T.R., Inoue, Y. and Vidal, A., 1994. Estimating crop water deficit using the relation between surface-air temperature and spectral vegetation index. Remote Sensing of Environment, 49: 246-263.

Morsdorf, F., Kotz, B., Meier, E., Itten, K.I. and Allgower, B., 2006. Estimation of LAI and fractional cover from small footprint airborne laser scanning data based on gap fraction. Remote Sensing of Environment, 104(1): 50-61.

Ohmura, A., 2005. Global energy and water balances. Encyclopedia of hydrological sciences, 5 Wiley & Sons, Chichester, 20 pp.

Ormsby, J.P., Choudhury, B.J., and Owe, M., 1987. Vegetation spatial variability and its effect on vegetation indices. International Journal of Remote Sensing, 8, 1301-1306 pp.

Peng, G., Ruiliang, P., Biging, G.S. and Larrieu, M.R., 2003. Estimation of forest leaf area index using vegetation indices derived from hyperion hyperspectral data. Geoscience and Remote Sensing, IEEE Transactions on, 41(6-part-1): 1355-1362.

Reithmaier, L.M., Gockede, M., Markkanen, T., Knohl, A., Churkina, G., Rebmann, C., Buchmann, N. and Foken, T., 2006. Use of remotely sensed land use classification for a better evaluation of micrometeorological flux measurement sites. Theoretical and Applied Climatology, 84(4): 219-233.

Salehi, F., Prasher, S.O., Amin, S., Madani, A., Jebelli, S. J., Ramaswamy, H.S., Tan, C. and Drury, C.F., 2000. Prediction of annual nitrate-N losses in drain outflows with artificial neural networks. Transactions of the Asae, 43(5): 1137-1143.

Singh, V.P., 1995. Environmental hydrology. Water science and technology, 15. Kluwer Academic, Dordrecht, 479 pp.

Su, Z., 2002. surface energy balance system SEBS for estimation of turbulent heat fluxes. Hydrology and earth system sciences (HESS), 6(1).

Su, Z., 2005. Estimation of the surface energy balance. Encyclopedia of hydrological sciences, 5. Wiley and Sons, Chichester, 50 pp.

Su, Z. and Jacobs, C., 2001. ENVISAT: Actual evaporation. Beleids Commissie Remote Sensing: USP-2 Report. Beleidscommissie Remote Sensing (BCRS), Delft, 57 pp.

Sugita, M. and Brutsaert, W., 1991. Daily Evaporation over a Region from Lower Boundary-Layer Profiles Measured with Radiosondes. Water Resources Research, 27(5): 747-752.

Vacchiano, G., Tonon, G., Panzacchi, P., Muzzi, E. and Motta, R., 2006. Comparison of optical and digital techniques for light microclimate assessment in the Paneveggio Forest, Trentino, Italy. Forest Ecology and Management, 3(2): 191-204.

Verstraeten, W.W., Veroustraete, F. and Feyen, J., 2005. Estimating evapotranspiration of European forests from NOAA-imagery at satellite overpass time: Towards an operational processing chain for integrated optical and thermal sensor data products. Remote Sensing of Environment, 96(2): 256-276.

Verstraeten, W.W., Veroustraete, F., Heyns, W., Roey, T.V. and Feyen, J., 2008. On uncertainties in carbon flux modelling and remotely sensed data assimilation: The Brasschaat pixel case. Advances in Space Research, 41(1): 20-35.

Zhang, Y., Chen, J.M. and Miller, J.R., 2005. Determining digital hemispherical photograph exposure for leaf area index estimation. Agricultural and Forest Meteorology, 133(1-4): 166-181.

Zhu, J.P. and Bettinger, P., 2008. Estimating the effects of adjacency and green-up constraints on landowners of different sizes and spatial arrangements located in the southeastern US. Forest Policy and Economics, 10(5): 295-302.

Appendices

Appendix 1A: Scatter plot showing relationship between hourly wind speed (measured at Haarweg site), LE and H (measured at Loobos site).

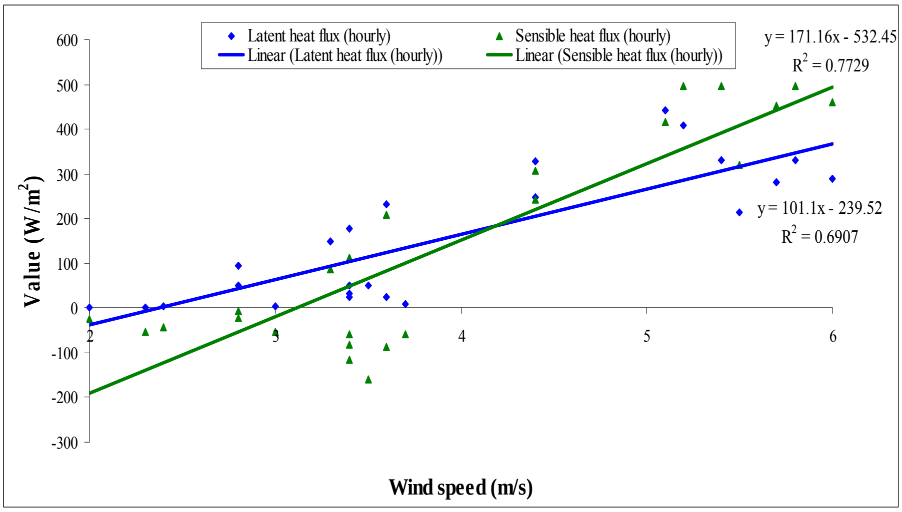

RMSE for LE is 50 W/m^2 for hourly values of 7 days.

Appendix 1B : Measured versus estimated values of LE for Loobos forest from the expression developed in Appendix 1A of LE.

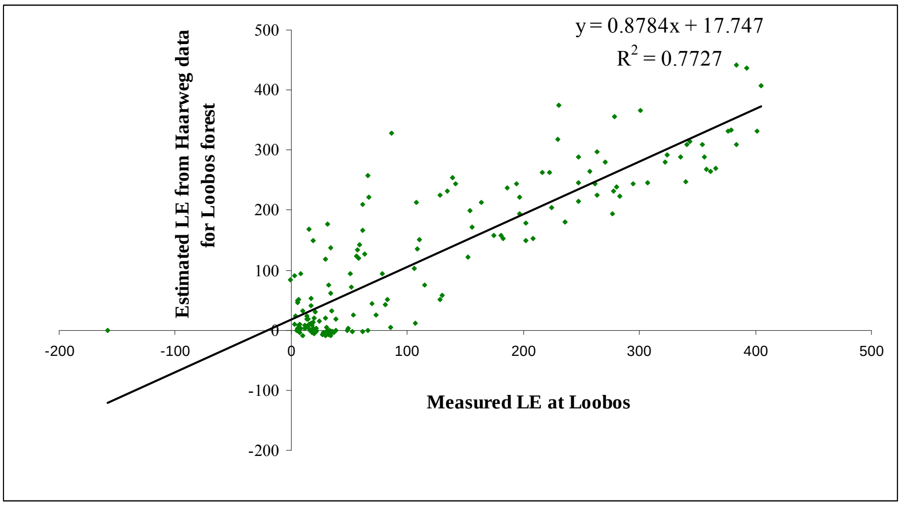

Appendix 2: Map showing location of three flux towers and sampling points where digital hemispherical photgraphs (DHP) were collected.

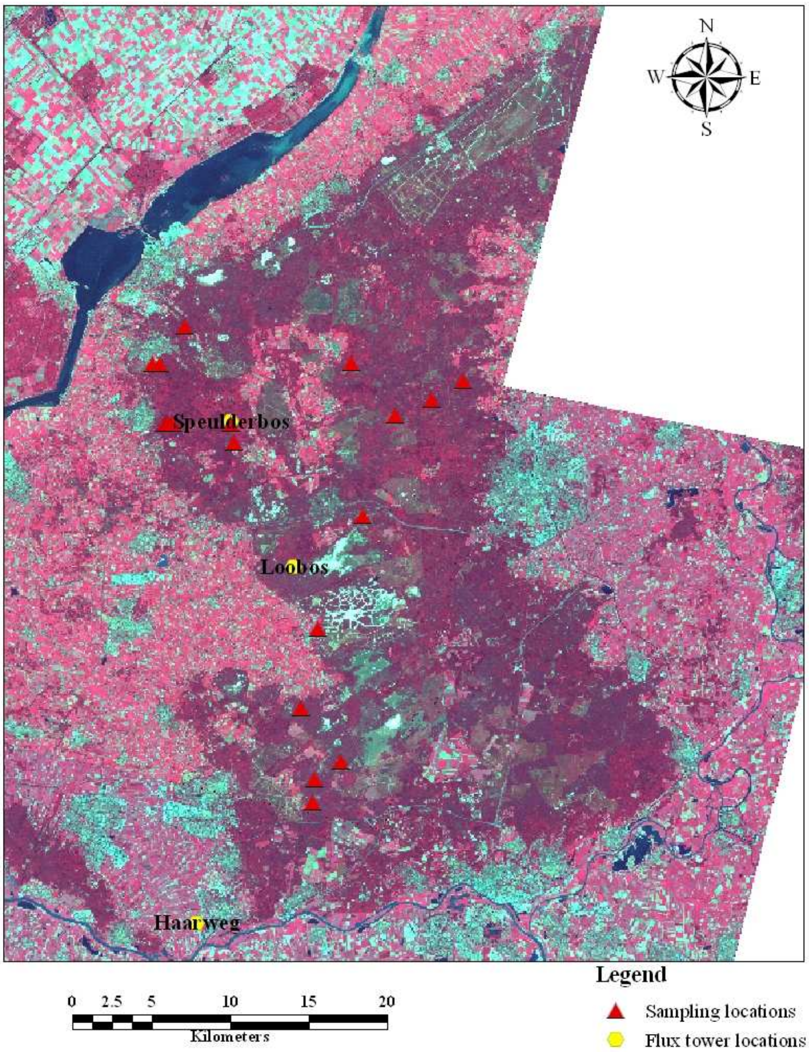

Appendix 3: Maps showing instantaneous LE in (W/m2) over Veluwe forest ridge, Netherlands. 1-Image of 30th Aug.2008, 2-Image of 27th June. 2008, 3-Image of 2nd June 2007 and 4-14th Aug. 2008.

1

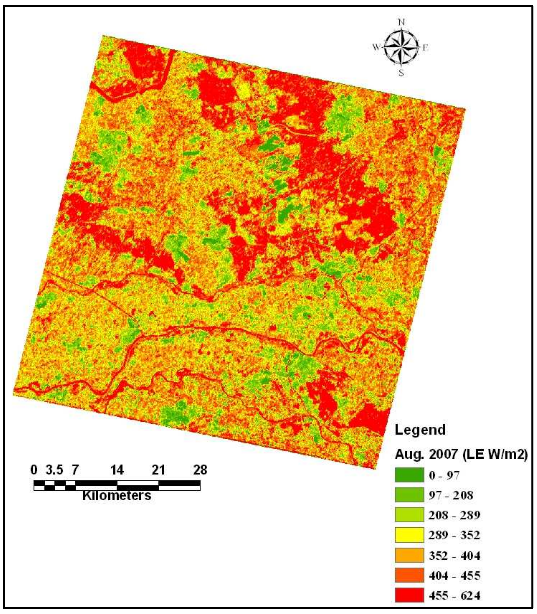

2

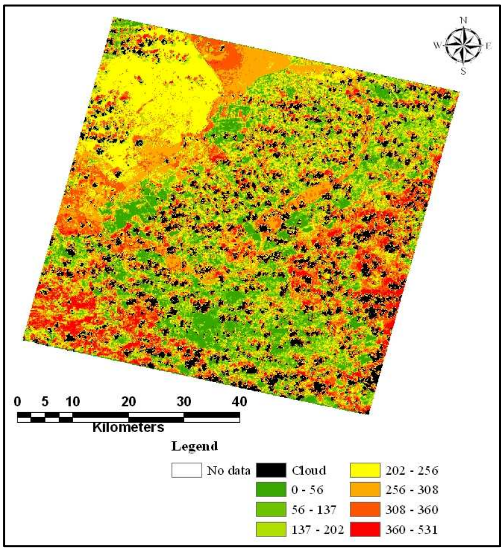

3

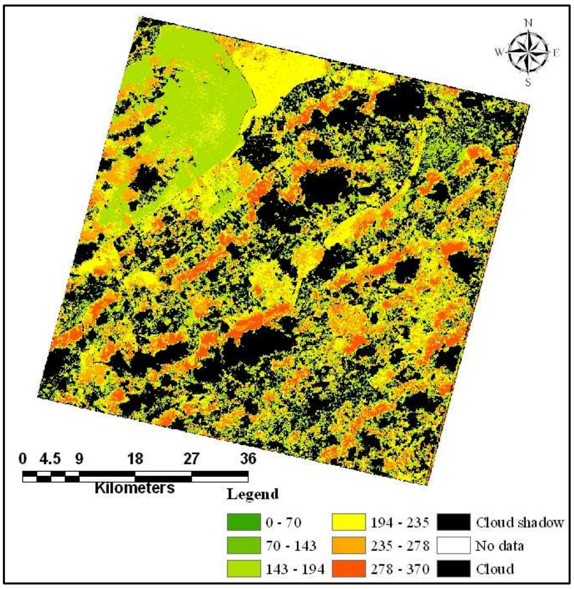
N
W
E
S
0
4.5
9
18
27
36
Kilometers
Legend
0 - 70
70 - 143
143 - 194
194 - 235
235 - 278
278 - 370
Cloud shadow
No data
Cloud

4

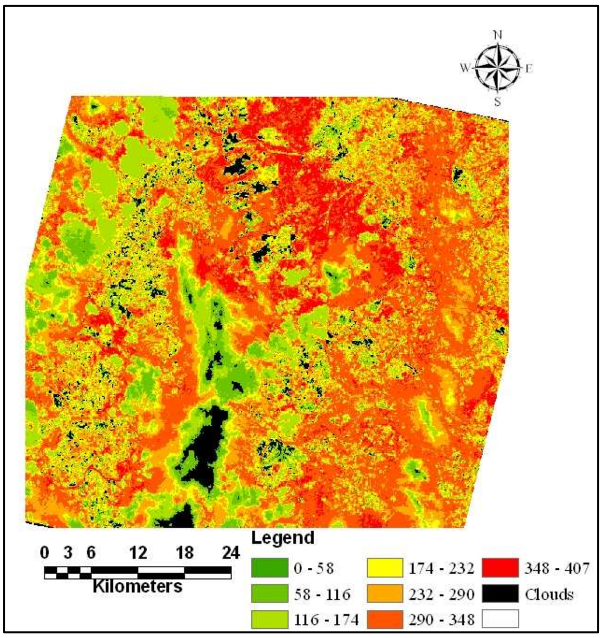
N
W
E
S
0
3
6
12
18
24
Kilometers
Legend
0 - 58
58 - 116
116 - 174
174 - 232
232 - 290
290 - 348
348 - 407
Clouds

Appendix 4: Digital hemispherical photographs taken during field data collection for estimation of fractional vegetation cover.

Image taken at 1/250 seconds exposure
Broad leaf forest

Image taken at 1/800 seconds exposure
Broad leaf forest

Image taken at 1/1000 seconds exposure
Broad leaf forest

Image taken at 1/250 seconds exposure
Coniferous forest

Image taken at 1/800 seconds exposure
Coniferous forest

Image taken at 1/1000 seconds exposure
Coniferous forest

Appendix 4: Programme to generate input maps for SEBS model

```
-------------------------------------------------------------------------------
 Surface Energy Balance System.py
 Created on: Thu Dec 25 2008 12:03:46 PM
 (generated by Anupam Badola, GEM 2007 student for M.Sc. Thesis work)
 -------------------------------------------------------------------------

 Import system modules
import arcgisscripting

 Create the Geoprocessor object
gp = arcgisscripting.create()

 Check out any necessary licenses
gp.CheckOutExtension("spatial")

 Allow overwrite output
gp.overwriteoutput = 1

try:
  # Set the input raster dataset
   inRaster = "D:/Base data/5128GRID/grid"
      # Set the output raster name
   outRaster = “D:/ILWIS_input/5128/”

      # Set constants for albedo calculation
   Constant1 = "0.484"
   Constant2 = "0.335"
   Constant3 = "0.324"
   Constant4 = "0.551"
   Constant5 = "0.305"
   Constant6 = "0.367"
   Constant7 = "0.0015"
   Constant8 = "1000"

   # Scaling of land suraface temperature and emissivity data
   gp.Times_sa(inRaster14, "0.001", EM)
   gp.Times_sa(inRaster15, "0.1", LST)
   gp.Minus_sa(LST, "273.15", LSTcel)
```

```
# Process: Albedo calculation for Band 1 of ASTER image
gp.Times_sa(Constant1, inRaster1, outRaster1)
# Process: Albedo calculation for Band 3 ASTER image
gp.Times_sa(Constant2, inRaster3, outRaster3)
# Process: Albedo calculation for Band 5 ASTER image
gp.Times_sa(Constant3, inRaster5, outRaster5)
# Process: Albedo calculation for Band 6 ASTER image
gp.Times_sa(Constant4, inRaster6, outRaster6)
# Process: Albedo calculation for Band 8 ASTER image
gp.Times_sa(Constant5, inRaster8, outRaster8)
# Process: Albedo calculation for Band 9 ASTER image
gp.Times_sa(Constant6, inRaster9, outRaster9)
# Process: Shortwave albedo calculation of image step 1 of 9
gp.Plus_sa(outRaster1, inRaster3, outRaster10)
# Process: Shortwave albedo calculation of image step 2 of 9
gp.Minus_sa(outRaster10, outRaster5, outRaster11)
# Process: Shortwave albedo calculation of image step 3 of 9
gp.Plus_sa(outRaster11, outRaster6, outRaster12)
# Process: Shortwave albedo calculation of image step 4 pf 9
gp.Plus_sa(outRaster12, outRaster8, outRaster13)
# Process: Shortwave albedo calculation of image step 5 pof 9
gp.Minus_sa(outRaster13, outRaster9, outRaster14)
# Process: Shortwave albedo calculation of image step 6 of 9
gp.Minus_sa(outRaster14, Constant7, outRaster15)
# Process: Shortwave albedo calculation of image step 7 of 9
gp.Greaterthanequal_sa(outRaster15, 0, outRaster16)
# Process: Shortwave albedo calculation of image step 8 of 9
gp.Times_sa(outRaster16, outRaster15, outRaster17)
# Process: Shortwave albedo calculation of image step 9 of 9
gp.Divide_sa(outRaster17, Constant8, Albedo)

# Set constants for calculation of soil heat flux
NDVIs = "0.14"
NDVIv = "0.9028"

# Calculation of NDVI
gp.Minus_sa(inRaster3, inRaster2, outRaster19)
gp.Plus_sa(inRaster3, inRaster2, outRaster20)
```

```
    gp.Divide_sa(outRaster19, outRaster20, NDVI)

    # Calculation of fractional cover using Gutman and Ignatov method and its compliment
    gp.Times_sa(outRaster17, 0, outRaster18)
    gp.Plus_sa(outRaster18, 1, outRaster101)
    gp.Times_sa(outRaster101, NDVIs, outRaster102)
    gp.Times_sa(outRaster101, NDVIv, outRaster103)
    gp.Minus_sa(outRaster103, outRaster102, NDVIvs)
    gp.Minus_sa(NDVI, NDVIs, outRaster21)
    gp.Divide_sa(outRaster21, NDVIvs, Fc)

    # Extraction of files in ASCII format
    gp.RasterToASCII_conversion(NDVI, NDVIA)
    gp.RasterToASCII_conversion(Fc, FcA)
    gp.RasterToASCII_conversion(Albedo, AlbedoA)
    gp.RasterToASCII_conversion(LST, LSTA)
    gp.RasterToASCII_conversion(EM, EMA)

    # Ceating layers for sensitivity analysis of emissivity
    gp.Times_sa(EM, "0.50", EMA_50)
    gp.Times_sa(EM, "0.40", EMA_40)
    gp.Times_sa(EM, "0.30", EMA_30)
    gp.Times_sa(EM, "0.20", EMA_20)
    gp.Times_sa(EM, "0.10", EMA_10)
    gp.Plus_sa(EM, EMA_50, EMA_51)
    gp.Plus_sa(EM, EMA_40, EMA_41)
    gp.Plus_sa(EM, EMA_30, EMA_31)
    gp.Plus_sa(EM, EMA_20, EMA_21)
    gp.Plus_sa(EM, EMA_10, EMA_11)
    gp.Minus_sa(EM, EMA_50, EMA_49)
    gp.Minus_sa(EM, EMA_40, EMA_39)
    gp.Minus_sa(EM, EMA_30, EMA_29)
    gp.Minus_sa(EM, EMA_20, EMA_19)
    gp.Minus_sa(EM, EMA_10, EMA_09)

    # Creating layers for sensitivity analysis of Fractional cover
    gp.Times_sa(Fc, "0.50", FCA_50)
    gp.Times_sa(Fc, "0.40", FCA_40)
```

```
gp.Times_sa(Fc, "0.30", FCA_30)
gp.Times_sa(Fc, "0.20", FCA_20)
gp.Times_sa(Fc, "0.10", FCA_10)
gp.Plus_sa(Fc, FCA_50, FCA_51)
gp.Plus_sa(Fc, FCA_40, FCA_41)
gp.Plus_sa(Fc, FCA_30, FCA_31)
gp.Plus_sa(Fc, FCA_20, FCA_21)
gp.Plus_sa(Fc, FCA_10, FCA_11)
gp.Minus_sa(Fc, FCA_50, FCA_49)
gp.Minus_sa(Fc, FCA_40, FCA_39)
gp.Minus_sa(Fc, FCA_30, FCA_29)
gp.Minus_sa(Fc, FCA_20, FCA_19)
gp.Minus_sa(Fc, FCA_10, FCA_09)

# Ceating layers for sensitivity analysis of LST
gp.Times_sa(LSTcel, "0.50", LSTA_50)
gp.Times_sa(LSTcel, "0.40", LSTA_40)
gp.Times_sa(LSTcel, "0.30", LSTA_30)
gp.Times_sa(LSTcel, "0.20", LSTA_20)
gp.Times_sa(LSTcel, "0.10", LSTA_10)
gp.Plus_sa(LSTcel, LSTA_50, LSTA_51B)
gp.Plus_sa(LSTA_51B, "273.15", LSTA_51)
gp.Plus_sa(LSTcel, LSTA_40, LSTA_41B)
gp.Plus_sa(LSTA_41B, "273.15", LSTA_41)
gp.Plus_sa(LSTcel, LSTA_30, LSTA_31B)
gp.Plus_sa(LSTA_31B, "273.15", LSTA_31)
gp.Plus_sa(LSTcel, LSTA_20, LSTA_21B)
gp.Plus_sa(LSTA_21B, "273.15", LSTA_21)
gp.Plus_sa(LSTcel, LSTA_10, LSTA_11B)
gp.Plus_sa(LSTA_11B, "273.15", LSTA_11)
gp.Minus_sa(LSTcel, LSTA_50, LSTA_49B)
gp.Plus_sa(LSTA_49B, "273.15", LSTA_49)
gp.Minus_sa(LSTcel, LSTA_40, LSTA_39B)
gp.Plus_sa(LSTA_39B, "273.15", LSTA_39)
gp.Minus_sa(LSTcel, LSTA_30, LSTA_29B)
gp.Plus_sa(LSTA_29B, "273.15", LSTA_29)
gp.Minus_sa(LSTcel, LSTA_20, LSTA_19B)
gp.Plus_sa(LSTA_19B, "273.15", LSTA_19)
gp.Minus_sa(LSTcel, LSTA_10, LSTA_09B)
```

```
gp.Plus_sa(LSTA_09B, "273.15", LSTA_09)

# Ceating layers for sensitivity analysis of Albedo
gp.Times_sa(Albedo, "0.50", AlbedoA_50)
gp.Times_sa(Albedo, "0.40", AlbedoA_40)
gp.Times_sa(Albedo, "0.30", AlbedoA_30)
gp.Times_sa(Albedo, "0.20", AlbedoA_20)
gp.Times_sa(Albedo, "0.10", AlbedoA_10)
gp.Plus_sa(Albedo, AlbedoA_50, AlbedoA_51)
gp.Plus_sa(Albedo, AlbedoA_40, AlbedoA_41)
gp.Plus_sa(Albedo, AlbedoA_30, AlbedoA_31)
gp.Plus_sa(Albedo, AlbedoA_20, AlbedoA_21)
gp.Plus_sa(Albedo, AlbedoA_10, AlbedoA_11)

gp.Minus_sa(Albedo, AlbedoA_50, AlbedoA_49)
gp.Minus_sa(Albedo, AlbedoA_40, AlbedoA_39)
gp.Minus_sa(Albedo, AlbedoA_30, AlbedoA_29)
gp.Minus_sa(Albedo, AlbedoA_20, AlbedoA_19)
gp.Minus_sa(Albedo, AlbedoA_10, AlbedoA_09)

# Ceating layers for sensitivity analysis of NDVI
gp.Times_sa(NDVI, "0.50", NDVIA_50)
gp.Times_sa(NDVI, "0.40", NDVIA_40)
gp.Times_sa(NDVI, "0.30", NDVIA_30)
gp.Times_sa(NDVI, "0.20", NDVIA_20)
gp.Times_sa(NDVI, "0.10", NDVIA_10)
gp.Plus_sa(NDVI, NDVIA_50, NDVIA_51)
gp.Plus_sa(NDVI, NDVIA_40, NDVIA_41)
gp.Plus_sa(NDVI, NDVIA_30, NDVIA_31)
gp.Plus_sa(NDVI, NDVIA_20, NDVIA_21)
gp.Plus_sa(NDVI, NDVIA_10, NDVIA_11)
gp.Minus_sa(NDVI, NDVIA_50, NDVIA_49)
gp.Minus_sa(NDVI, NDVIA_40, NDVIA_39)
gp.Minus_sa(NDVI, NDVIA_30, NDVIA_29)
gp.Minus_sa(NDVI, NDVIA_20, NDVIA_19)
gp.Minus_sa(NDVI, NDVIA_10, NDVIA_09)
gp.RasterToASCII_conversion(AlbedoA_51, AlbedoA_51A)
gp.RasterToASCII_conversion(AlbedoA_41, AlbedoA_41A)
gp.RasterToASCII_conversion(AlbedoA_31, AlbedoA_31A)
```

```
gp.RasterToASCII_conversion(AlbedoA_21, AlbedoA_21A)
gp.RasterToASCII_conversion(AlbedoA_11, AlbedoA_11A)
gp.RasterToASCII_conversion(AlbedoA_49, AlbedoA_49A)
gp.RasterToASCII_conversion(AlbedoA_39, AlbedoA_39A)
gp.RasterToASCII_conversion(AlbedoA_29, AlbedoA_29A)
gp.RasterToASCII_conversion(AlbedoA_19, AlbedoA_19A)
gp.RasterToASCII_conversion(AlbedoA_09, AlbedoA_09A)
gp.RasterToASCII_conversion(NDVIA_51, NDVIA_51A)
gp.RasterToASCII_conversion(NDVIA_41, NDVIA_41A)
gp.RasterToASCII_conversion(NDVIA_31, NDVIA_31A)
gp.RasterToASCII_conversion(NDVIA_21, NDVIA_21A)
gp.RasterToASCII_conversion(NDVIA_11, NDVIA_11A)
gp.RasterToASCII_conversion(NDVIA_49, NDVIA_49A)
gp.RasterToASCII_conversion(NDVIA_39, NDVIA_39A)
gp.RasterToASCII_conversion(NDVIA_29, NDVIA_29A)
gp.RasterToASCII_conversion(NDVIA_19, NDVIA_19A)
gp.RasterToASCII_conversion(NDVIA_09, NDVIA_09A)
gp.RasterToASCII_conversion(EMA_51, EMA_51A)
gp.RasterToASCII_conversion(EMA_41, EMA_41A)
gp.RasterToASCII_conversion(EMA_31, EMA_31A)
gp.RasterToASCII_conversion(EMA_21, EMA_21A)
gp.RasterToASCII_conversion(EMA_11, EMA_11A)
gp.RasterToASCII_conversion(EMA_49, EMA_49A)
gp.RasterToASCII_conversion(EMA_39, EMA_39A)
gp.RasterToASCII_conversion(EMA_29, EMA_29A)
gp.RasterToASCII_conversion(EMA_19, EMA_19A)
gp.RasterToASCII_conversion(EMA_09, EMA_09A)
gp.RasterToASCII_conversion(LSTA_51, LSTA_51A)
gp.RasterToASCII_conversion(LSTA_41, LSTA_41A)
gp.RasterToASCII_conversion(LSTA_31, LSTA_31A)
gp.RasterToASCII_conversion(LSTA_21, LSTA_21A)
gp.RasterToASCII_conversion(LSTA_11, LSTA_11A)
gp.RasterToASCII_conversion(LSTA_49, LSTA_49A)
gp.RasterToASCII_conversion(LSTA_39, LSTA_39A)
gp.RasterToASCII_conversion(LSTA_29, LSTA_29A)
gp.RasterToASCII_conversion(LSTA_19, LSTA_19A)
gp.RasterToASCII_conversion(LSTA_09, LSTA_09A)
gp.RasterToASCII_conversion(FCA_51, FCA_51A)
gp.RasterToASCII_conversion(FCA_41, FCA_41A)
```

```
    gp.RasterToASCII_conversion(FCA_31, FCA_31A)
    gp.RasterToASCII_conversion(FCA_21, FCA_21A)
    gp.RasterToASCII_conversion(FCA_11, FCA_11A)
    gp.RasterToASCII_conversion(FCA_49, FCA_49A)
    gp.RasterToASCII_conversion(FCA_39, FCA_39A)
    gp.RasterToASCII_conversion(FCA_29, FCA_29A)
    gp.RasterToASCII_conversion(FCA_19, FCA_19A)
    gp.RasterToASCII_conversion(FCA_09, FCA_09A)

except:
    # if an error occured while running a tool, then print the message.
    print gp.GetMessages()
```

Appendix 5: Programme to generate SEBS output Maps for ± 50% range of base input value.

Code for surface albedo is shown taking other inputs constant (Similarly, maps were generated for other variables (LST, NDVI, Fractional cover and surface emissivity).

```
cd D:\Base data\Final data\5128GRID\ILWIS_input\base value\
'5128'.mpr =
MapSEBS(lsta,ema,albedoa,ndvia,0,,1,fca,0,nomap,53.33,0,nomap,20,1,217,0,0,0,1
0,1000,0,,0.008,0,,5.1,0,,26,0,,101680,0,,100100,5,1,779,0,nomap)
open 'D:\Base data\Final data\5128GRID\ILWIS_input\base value\5128'.mpr

cd D:\Base data\Final data\5128GRID\ILWIS_input\5128A_09\
'5128A_09'.mpr =
MapSEBS(lsta,ema,albedoa_09,ndvia,0,,1,fca,0,nomap,53.33,0,nomap,20,1,217,0,0,
0,10,1000,0,,0.008,0,,5.1,0,,26,0,,101680,0,,100100,5,1,779,0,nomap)
open 'D:\Base data\Final data\5128GRID\ILWIS_input\5128A_09\5128A_09'.mpr

cd D:\Base data\Final data\5128GRID\ILWIS_input\5128A_11\
'5128A_11'.mpr =
MapSEBS(lsta,ema,albedoa_11,ndvia,0,,1,fca,0,nomap,53.33,0,nomap,20,1,217,0,0,
0,10,1000,0,,0.008,0,,5.1,0,,26,0,,101680,0,,100100,5,1,779,0,nomap)
open 'D:\Base data\Final data\5128GRID\ILWIS_input\5128A_11\5128A_11'.mpr

cd D:\Base data\Final data\5128GRID\ILWIS_input\5128A_19\
'5128A_19'.mpr =
MapSEBS(lsta,ema,albedoa_19,ndvia,0,,1,fca,0,nomap,53.33,0,nomap,20,1,217,0,0,
0,10,1000,0,,0.008,0,,5.1,0,,26,0,,101680,0,,100100,5,1,779,0,nomap)
open 'D:\Base data\Final data\5128GRID\ILWIS_input\5128A_19\5128A_19'.mpr

cd D:\Base data\Final data\5128GRID\ILWIS_input\5128A_21\
'5128A_21'.mpr =
MapSEBS(lsta,ema,albedoa_21,ndvia,0,,1,fca,0,nomap,53.33,0,nomap,20,1,217,0,0,
0,10,1000,0,,0.008,0,,5.1,0,,26,0,,101680,0,,100100,5,1,779,0,nomap)
open 'D:\Base data\Final data\5128GRID\ILWIS_input\5128A_21\5128A_21'.mpr

cd D:\Base data\Final data\5128GRID\ILWIS_input\5128A_29\
```

```
'5128A_29'.mpr =
MapSEBS(lsta,ema,albedoa_29,ndvia,0,,1,fca,0,nomap,53.33,0,nomap,20,1,217,0,0,
0,10,1000,0,,0.008,0,,5.1,0,,26,0,,101680,0,,100100,5,1,779,0,nomap)
open 'D:\Base data\Final data\5128GRID\ILWIS_input\5128A_29\5128A_29'.mpr

cd D:\Base data\Final data\5128GRID\ILWIS_input\5128A_31\
'5128A_31'.mpr =
MapSEBS(lsta,ema,albedoa_31,ndvia,0,,1,fca,0,nomap,53.33,0,nomap,20,1,217,0,0,
0,10,1000,0,,0.008,0,,5.1,0,,26,0,,101680,0,,100100,5,1,779,0,nomap)
open 'D:\Base data\Final data\5128GRID\ILWIS_input\5128A_31\5128A_31'.mpr

cd D:\Base data\Final data\5128GRID\ILWIS_input\5128A_39\
'5128A_39'.mpr =
MapSEBS(lsta,ema,albedoa_39,ndvia,0,,1,fca,0,nomap,53.33,0,nomap,20,1,217,0,0,
0,10,1000,0,,0.008,0,,5.1,0,,26,0,,101680,0,,100100,5,1,779,0,nomap)
open 'D:\Base data\Final data\5128GRID\ILWIS_input\5128A_39\5128A_39'.mpr

cd D:\Base data\Final data\5128GRID\ILWIS_input\5128A_41\
'5128A_41'.mpr =
MapSEBS(lsta,ema,albedoa_41,ndvia,0,,1,fca,0,nomap,53.33,0,nomap,20,1,217,0,0,
0,10,1000,0,,0.008,0,,5.1,0,,26,0,,101680,0,,100100,5,1,779,0,nomap)
open 'D:\Base data\Final data\5128GRID\ILWIS_input\5128A_41\5128A_41'.mpr

cd D:\Base data\Final data\5128GRID\ILWIS_input\5128A_49\
'5128A_49'.mpr =
MapSEBS(lsta,ema,albedoa_49,ndvia,0,,1,fca,0,nomap,53.33,0,nomap,20,1,217,0,0,
0,10,1000,0,,0.008,0,,5.1,0,,26,0,,101680,0,,100100,5,1,779,0,nomap)
open 'D:\Base data\Final data\5128GRID\ILWIS_input\5128A_49\5128A_49'.mpr

cd D:\Base data\Final data\5128GRID\ILWIS_input\5128A_51\
'5128A_51'.mpr =
MapSEBS(lsta,ema,albedoa_51,ndvia,0,,1,fca,0,nomap,53.33,0,nomap,20,1,217,0,0,
0,10,1000,0,,0.008,0,,5.1,0,,26,0,,101680,0,,100100,5,1,779,0,nomap)
open 'D:\Base data\Final data\5128GRID\ILWIS_input\5128A_51\5128A_51'.mpr
```